Thalamocortical excitability adjustments guide human perception under uncertainty

Julian Q. Kosciessa[1,2,3]*, Ulman Lindenberger[1,2], Douglas D. Garrett[1,2]*

[1]Max Planck UCL Centre for Computational Psychiatry and Ageing Research, Berlin and London; [2]Center for Lifespan Psychology, Max Planck Institute for Human Development, Lentzeallee 94, 14195 Berlin, Germany. [3]Department of Psychology, Humboldt-Universität zu Berlin, Berlin, Germany

Julian Q. Kosciessa: https://orcid.org/0000-0002-4553-2794
Ulman Lindenberger: https://orcid.org/0000-0001-8428-6453
Douglas D. Garrett: https://orcid.org/0000-0002-0629-7672

* Correspondence:

kosciessa@mpib-berlin.mpg.de (Lead Contact); garrett@mpib-berlin.mpg.de

Abstract

Adaptive human behavior builds on prior knowledge about stimulus relevance. Some environments cue such knowledge more than others. To behave adaptively, observers need to flexibly adjust sensory processing to the degree of contextual uncertainty. We hypothesize that the neural basis for these perceptual adjustments consists in the ability of the cortical network to switch back and forth between a rhythmic state that serves selective processing, and a state of elevated asynchronous neural activity that boosts sensitivity. To test this hypothesis, we recorded non-invasive EEG and fMRI BOLD dynamics while 47 healthy young adults performed a parametric visual attention task with varying numbers of relevant stimulus features. Drift-diffusion modeling of response behavior and electrophysiological signatures revealed that greater contextual uncertainty lowered the rate of evidence accumulation while increasing thalamocortical engagement, with concomitant increments in cortical excitability and pupil dilation. As predicted, uncertainty-related processing adjustments were expressed as switches between a state of phase-dependent excitability modulation in the alpha band and a state of increased irregularity of brain dynamics. We conclude that humans dynamically adjust sensory excitability according to the processing fidelity afforded by an upcoming choice, and that neuromodulatory processes involving the thalamus play a key role in adjusting excitability in the human brain.

Highlights

- With increasing contextual uncertainty, human cortical networks shift from a state of phase-dependent excitability modulation in the alpha band into a state of elevated excitatory tone and asynchronous neural activity

- Evidence based on joint modeling of behavior, EEG, and BOLD suggests that neuromodulatory processes involving the thalamus regulate these shifts

- Theoretical and empirical considerations suggest contributions of both frequency-specific and aperiodic neural dynamics to human behavior

Introduction

Adaptive behavior requires dynamic adjustments to the perception of high-dimensional inputs. Prior knowledge about the momentary relevance of specific environmental features selectively enhances their processing while suppressing distractors (for reviews see Buschman & Kastner, 2015; Desimone & Duncan, 1995; Maunsell, 2015), which can be implemented via gain modulation in sensory cortex (Ferguson & Cardin, 2020). Crucially, *a priori* information regarding feature relevance is not always available; and how the brain flexibly adjusts the processing of complex inputs according to contextual uncertainty remains unclear (Bach & Dolan, 2012).

Selective gain control has been associated with ***phasic*** (i.e., phase-dependent) inhibition of task-irrelevant stimulus dimensions during cortical alpha (˜8-12 Hz) rhythms (Klimesch, Sauseng, & Hanslmayr, 2007; Sadaghiani & Kleinschmidt, 2016). In particular, rhythmic modulations of feedforward excitability (Haegens, Nacher, Luna, Romo, & Jensen, 2011; Lorincz, Kekesi, Juhasz, Crunelli, & Hughes, 2009) may provide temporal 'windows of opportunity' for high-frequency gamma synchronization in sensory cortex (Spaak, Bonnefond, Maier, Leopold, & Jensen, 2012; van Kerkoerle et al., 2014) and increased sensory gain (Fries, 2015; Ni et al., 2016; Peterson & Voytek, 2017). However, specifically increasing the fidelity of single stimulus dimensions is theoretically insufficient when uncertain environments require joint sensitivity to multiple stimulus features (Pettine, Louie, Murray, & Wang, 2020). During high uncertainty, transient increases to the ***tonic*** excitation/inhibition (E/I) ratio in sensory cortex provide a principled mechanism for elevated sensitivity to – and a more faithful processing of – high-dimensional stimuli (Destexhe, Rudolph, & Pare, 2003; Marguet & Harris, 2011). In electrophysiological recordings, scale-free 1/f slopes are sensitive to differences in E/I ratio (Gao, Peterson, & Voytek, 2017), and vary alongside sensory stimulation (Billig et al., 2019; Podvalny et al., 2015) and arousal states (Colombo et al., 2019; Lendner et al., 2019). Whether contextual demands modulate scale-free activity is unknown however. We hypothesize that high uncertainty shifts cortical regimes from rhythmic excitability modulations towards tonic excitability increases.

Such state switches in network excitability may be shaped by neuromodulation and subcortical activity (Harris & Thiele, 2011). Neuromodulation potently alters cortical states (Froemke, 2015; Thiele & Bellgrove, 2018) and sensory processing (Berridge & Waterhouse, 2003; McCormick, Pape, & Williamson, 1991; McGinley, David, & McCormick, 2015), and noradrenergic arousal in particular may permit high sensitivity to incoming stimuli (Posner & Rothbart, 2007). Yet, non-invasive evidence is lacking for whether/how neuromodulation affects contextual adaptability. Moreover, despite early proposals for thalamic involvement in attentional control (Crick, 2003; Jasper, 1948; Rafal & Posner, 1987), studies have dominantly focused on cortical information flow (e.g., Siegel, Buschman, & Miller, 2015), at least in part due to technical difficulties in characterizing thalamic contributions. Crucially, the thalamus provides a nexus for the contextual modulation of cortical circuits (Halassa & Kastner, 2017; Honjoh et al., 2018), is a key component of neuromodulatory networks (McCormick et al., 1991; Schiff, 2008; Song et al., 2017) and robustly modulates system excitability via rhythmic and aperiodic membrane fluctuations (Jones, 2009). However, human evidence for a central thalamic role in cortical state adjustments at the service of behavioral flexibility is missing.

45 Here, we aimed at overcoming this lacuna by assessing the effects of contextual uncertainty
46 during stimulus encoding on cortical excitability, neuromodulation, and thalamic activity in
47 humans. We performed a multi-modal (parallel) EEG-fMRI experiment to capture both fast
48 cortical dynamics (EEG) and subcortical activity (fMRI) while recording pupil dilation as a
49 non-invasive proxy for neuromodulatory drive (Joshi & Gold, 2020). Participants performed a
50 parametric adaptation of the classic dot motion task (Gold & Shadlen, 2007) (Figure 1).
51 Specifically, we manipulated the number of stimulus dimensions that are task-relevant in a
52 given trial while holding the sensory features of the task (i.e., its appearance on the screen)
53 constant across trials. By applying drift-diffusion modeling to participants' choice behavior
54 while jointly assessing electrophysiological signatures of decision processes, we found that
55 uncertainty during sensation reduces the rate of subsequent evidence integration. This
56 reduction in available sensory evidence for single targets was associated with increased
57 cortical excitability, as indexed by joint low-frequency (~alpha) desynchronization and high-
58 frequency (~gamma) synchronization, and an increase in E/I ratio, as indicated by increased
59 sample entropy and flatter scale-free 1/f slopes, during stimulus processing, in lines with
60 broad sensitivity increases during periods of higher uncertainty. These excitability
61 adjustments occurred in parallel with increases in pupil-based arousal. Finally, inter-
62 individual differences in the modulation of cortical excitability, drift rates and arousal were
63 jointly associated with the extent of thalamic BOLD signal modulation, pointing to the
64 importance of subcortical mechanisms for cortical state adjustments. Together, these
65 findings suggest that neuromodulatory processes involving the thalamus shape cortical
66 excitability states in humans, and that a shift from alpha-rhythmic to aperiodic neural
67 dynamics adjusts the processing fidelity of external stimuli in service of upcoming decisions.

68
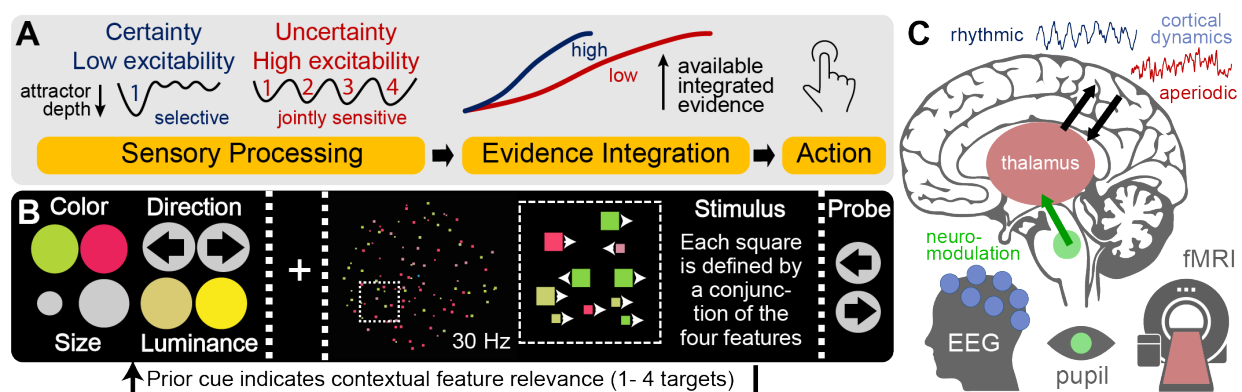
69 **Figure 1. Hypotheses & task design.** (**A**) We probed whether participants modulate cortical
70 excitability during stimulus processing to guide subsequent evidence accumulation. We hypothesized
71 that when valid attentional cues about a single target feature are available in advance, a low
72 excitability regime may optimize subsequent choices via the targeted selection of relevant – and
73 inhibition of irrelevant – information. This can be conceptualized as the creation of a "single feature
74 attractor." In contrast, under high probe uncertainty, higher excitability may afford the concurrent
75 sampling of multiple relevant features, but at the cost of a relative reduction of subsequently available
76 evidence for any individual feature. (**B**) Participants performed a **M**ulti-**A**ttribute **A**ttention **T**ask
77 ("MAAT") during which they had to sample up to four visual features in a joint display for immediate
78 subsequent recall. Prior to stimulus presentation, participants were validly cued to a set of potential
79 target probes. The number and identity of cues were varied to experimentally manipulate the level of
80 expected probe uncertainty. (**C**) We hypothesized that increasing probe uncertainty would induce a
81 joint increase in neuromodulation and thalamic activity, associated with shifts from a phasic gain
82 control mode (implemented via neural alpha rhythms) toward transient increases in tonic excitability
83 (as indicated by aperiodic cortical activity). Participants performed the same task in both an EEG and

84 an fMRI session, allowing us to assess joint inter-individual differences in fast cortical dynamics (EEG)
85 and subcortical sources (fMRI).

Results

87 We developed a dynamic visual **M**ulti-**A**ttribute **A**ttention **T**ask ("MAAT") to uncover rapid
88 adjustments to stimulus processing and perceptual decisions under expected uncertainty
89 (Figure 1). Participants visually sampled a moving display of small squares, which were
90 characterized by four stimulus features, with two exemplars each: their color (red/green),
91 their movement direction (left/right), their size (large/small), and their color saturation
92 (high/low). Any individual square was characterized by a conjunction of the four features,
93 while one exemplar of each feature (e.g., green color) was most prevalent in the entire
94 display. Following stimulus presentation, participants were probed on a single feature as to
95 which of the two exemplars was most prevalent (via 2-AFC). Probe uncertainty was
96 parametrically manipulated using valid pre-stimulus cues, indicating the feature set from
97 which a probe would be selected. The feature set remained constant for a sequence of eight
98 trials to reduce set switching demands. Optimal performance required flexible sampling of
99 the cued feature set while jointly inhibiting uncued features; participants had to thus rapidly
100 encode a varying number of targets ("target load") to prepare for an upcoming probe.
101 Participants performed the task well above chance level for different features and for different
102 levels of probe uncertainty (Figure S1A). As the number of relevant targets increased,
103 participants systematically became slower (median RT; EEG: β = .138, $p \sim 0$; MRI: β = .107,
104 $p \sim 0$) and less accurate (EEG: β = -.032, $p \sim 0$; MRI: β = -.025, p = 2.4e-07) in their
105 response to single-feature probes (Figure S1B).

Probe uncertainty during sensation decreases the rate of subsequent evidence integration

106 We leveraged the potential of sequential sampling models to disentangle separable decision
107 processes in order to assess their modulation by probe uncertainty. In particular, drift-
108 diffusion models estimate (a) the non-decision time (NDT), (b) the drift rate at which
109 information becomes available, and (c) the internal evidence threshold or boundary
110 separation (see Figure 2A; for a review see Forstmann, Ratcliff, & Wagenmakers, 2016). We
111 fitted a hierarchical drift-diffusion model (HDDM) separately for each testing session, and
112 assessed individual parameter convergence with established EEG signatures (Donner,
113 Siegel, Fries, & Engel, 2009; O'Connell, Dockree, & Kelly, 2012; Twomey, Kelly, &
114 O'Connell, 2016; van Vugt, Beulen, & Taatgen, 2019). In particular, we investigated the
115 Centroparietal Positive Potential (CPP) and lateralized beta suppression as established
116 neural signatures of evidence integration from eidetic memory traces (Twomey et al., 2016).
117 The best behavioral fit was obtained by a model incorporating probe uncertainty-based
118 variations in drift rate, non-decision time and boundary separation (Figure S1B). Yet, there
119 was no evidence for modulation of the threshold of the CPP or the contralateral beta
120 response (Figure S1C). In line with prior work (McGovern, Hayes, Kelly, & O'Connell, 2018),
121 we therefore selected an EEG-informed model with fixed thresholds across target load
122 levels. With this model, reliability of individual parameters as well as of their load-related
123 changes was high across EEG and MRI sessions (see below and Figure S1E, F). Parameter
124 interrelations are reported in Text S1.
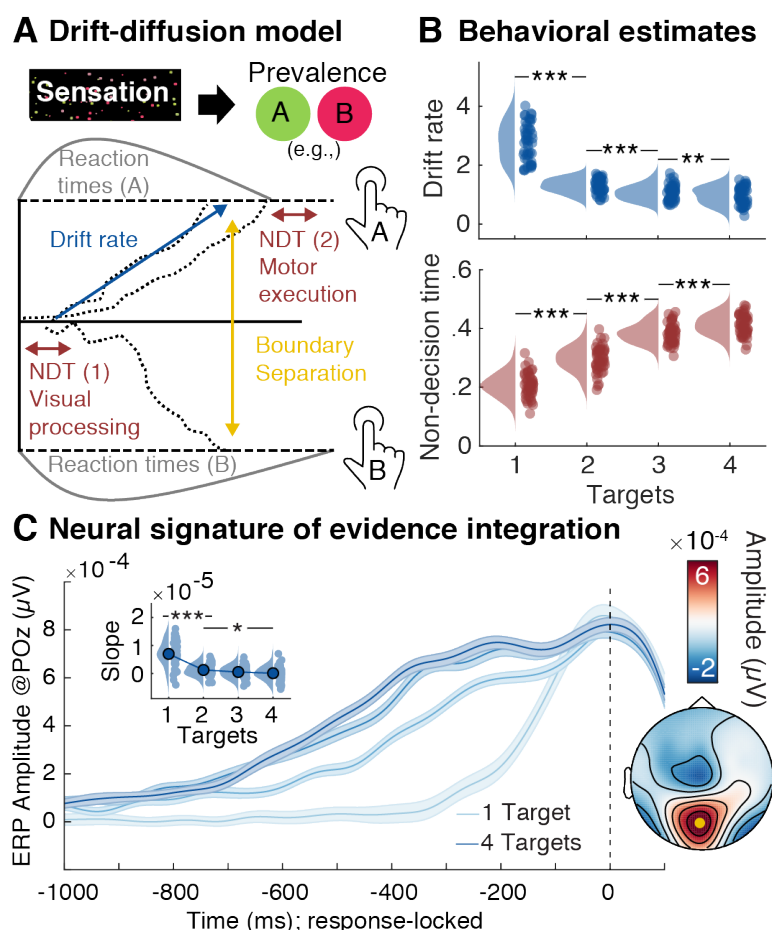
Figure 2: Evidence integration upon probe presentation decreases as a function of prior uncertainty. (**A**) Schematic of drift-diffusion model. Following visual encoding, evidence is successively accumulated towards either of two bounds when probed for the dominant prevalence of one of two options of a single feature. A button press indicates the decision once one of the bounds has been reached and motor preparation has concluded. A non-decision time parameter captures visual encoding and motor preparation, drift rate captures the amount of available information, and boundary separation captures response bias i.e., conservative vs. liberal). (**B**) Behavioral parameter estimates for drift rate and non-decision time (NDT; discussed in Text S3), as indicated by the hierarchical drift-diffusion model (HDDM). (**C**) Modulation of the Centroparietal Positive Potential (CPP) as a neural signature of evidence accumulation (mean +- within-subject SE). The probe-locked CPP indicates decreases in drift rate with prior probe uncertainty. Insets show CPP slope estimates from -250 to -100 ms relative to response execution, as well as the corresponding topography (CPP channel shown in yellow). [*** p < .001, ** p < .01, * p < .05]

Behavioral model estimates (Figure 2B) and EEG signatures (Figure 2C, Figure S2A) jointly indicated that probe uncertainty during stimulus presentation decreased the drift rate during subsequent evidence accumulation. This indicates a reduction of available evidence for single features when more features had to be sampled. Individual drift rate estimates for a single target were positively correlated with the slope of the CPP (r = 0.52, 95%CI [0.26, 0.71], p = 3.59e-4), while individual drift rate reductions reflected the shallowing of CPP slopes (r(137) = 0.34, 95%CI [0.18, 0.48], p = 4.87e-5). Notably, the magnitude of evidence decreases with increasing probe uncertainty was strongly anticorrelated with the available evidence when the target attribute was known in advance (i.e., the single target condition; EEG session: *r* = -.93, *p* = 4e-22, MRI session: *r* = -.88, *p* = 1e-15). That is, participants with more available evidence after selectively attending to a single target showed larger drift rate

5

150 decreases under increased probe uncertainty. Importantly however, participants with higher
151 drift rates for single targets also retained higher drift rates at higher probe uncertainty (i.e.,
152 high reliability for e.g., four targets: EEG: r = .48; p = 6e-4; MRI: r = .53, p = 2e-4). Moreover,
153 individuals with higher drift rates across target loads exhibited lower average RTs (EEG: $r = -$
154 $.42$, $p = .003$; MRI: $r = -.41$, $p = .007$) and higher task accuracy (EEG: $r = .86$, $p = $ 2e-14;
155 MRI: $r = .89$, $p = $ 4e-16). Thus, in the present paradigm, more pronounced drift rate
156 decreases with increasing probe uncertainty index a successful modulation of feature-based
157 attention during encoding, and better overall performance.

158 We performed multiple control analyses to further elucidate decision properties. First, we did
159 not observe a similar ramping of the CPP during stimulus presentation (Figure S2B),
160 suggesting that evidence accumulation was primarily initiated by the probe. Second, drift rate
161 reductions were not primarily driven by differences between feature attributes (Figure S2C).
162 Third, concurrent variations in response agreement across cued attributes could not account
163 for the observed effects (Text S2; Figure S1D). Fourth, individual drift rates for single targets
164 were unrelated to threshold estimates (EEG: $r = -.005$, $p = .74$; MRI: $r = -.006$; $p = .72$), thus
165 suggesting a lack of differences in response bias (Ratcliff & McKoon, 2008). Finally,
166 participants with larger drift rate decreases exhibited more constrained non-decision time
167 increases (EEG: r(137) = 0.32, 95% CI [0.16, 0.47], p = 1.04e-4; MRI: r(122) = 0.37, 95%CI
168 [0.2, 0.51], p = 2.48e-5), indicating reduced additional motor transformation demands (see
169 Text S3) in high performers.

Cortical excitability increases under uncertainty guide subsequent evidence integration

170 Decreases in the rate of evidence integration indicate the detrimental consequences of probe
171 uncertainty, but not the mechanisms by which sensory processing is altered. To investigate
172 the latter, we examined rhythmic and aperiodic cortical signatures during stimulus
173 processing. To jointly assess multivariate changes in spectral power as a function of probe
174 uncertainty, we performed a partial-least-squares (PLS) analysis that produces low-
175 dimensional, multivariate relations between brain-based data – in this case time-frequency-
176 space matrices – and other variables of interest (see methods). First, we assessed evoked
177 changes compared to baseline using a task PLS. We observed a single latent variable (LV;
178 permuted $p < .001$) with jointly increased power in the delta-theta and gamma bands and
179 decreased alpha power upon stimulus onset (Figure S3A, Figure S4A), in line with increased
180 cognitive control (Cavanagh & Frank, 2014) and heightened bottom-up visual processing
181 (van Kerkoerle et al., 2014). We next performed a task PLS to assess spectral power
182 changes as a function of target load. A single LV (permuted $p < .001$; Figure 3) indicated a
183 stronger expression of this control- and excitability-like pattern with increasing probe
184 uncertainty. Next, we assessed the link between individual changes in multivariate loadings
185 on this "spectral power modulation factor" (SPMF) and behavioral modulations. We
186 performed *partial repeated measures correlations (*see methods), a mixed modelling
187 approach that controls for the main effect of probe uncertainty in both variables of interest
188 and indicates interindividual associations independent of the specific shape of condition
189 modulation in individual participants. Crucially, individual SPMF loadings were positively
190 correlated with interindividual performance differences during selective attention (Figure 3F)
191 and uncertainty-related performance changes (Figure 3G). Participants with stronger spectral
192 power modulation during sensation exhibited faster evidence integration in the selective
193 attention condition, as well as a stronger drift rate decreases under uncertainty [r(137) = -0.4,

95%CI [-0.53, -0.25], p = 1.12e-6], while showing constrained increases in non-decision time [r(137) = -0.26, 95%CI [-0.41, -0.1], p ~ 0]. In sum, this suggests that high performers flexibly increased visual throughput as more features became relevant via top-down control of cortical excitability.
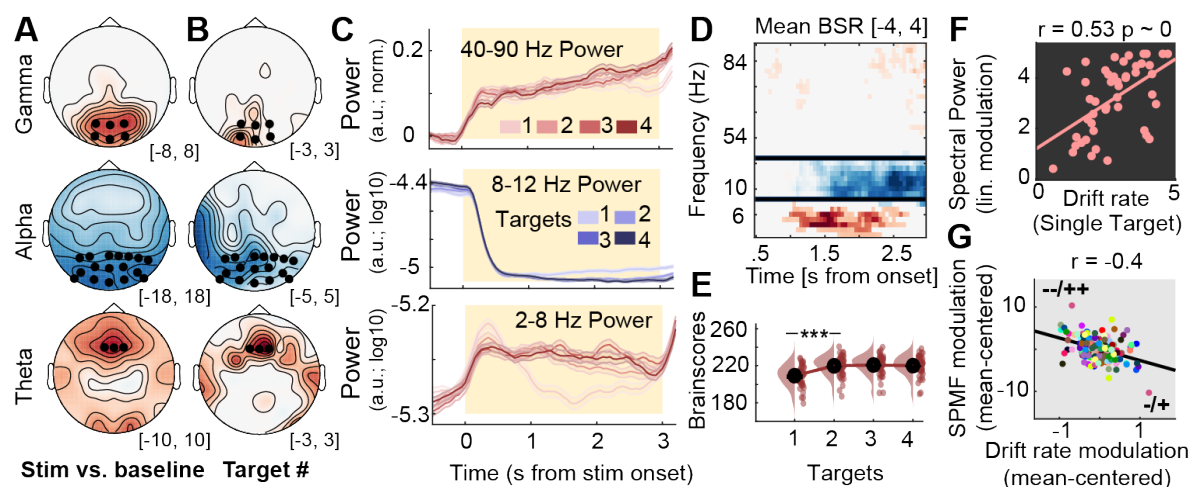

Figure 3: Multivariate power changes with probe uncertainty during stimulus encoding. (**A, B**) Topographies of stimulus-evoked power changes relative to pre-stimulus baseline (A, see Figure S3-1) and load-related power modulation (B). With increasing attentional demands, theta and 'broadband' gamma power increased, whereas alpha rhythms desynchronize. Asterisks indicate the sensors across which data were averaged for presentation in D. Values indicate maximum (theta/gamma) or minimum (alpha range) bootstrap ratios (BSR) across time in the clusters. (**C**) Temporal traces of band-limited power as a function of target load, extracted from the clusters presented in D (mean +- within-subject SE). (**D, E**) Multivariate loading pattern (D) for spectral power changes under uncertainty and associated multivariate brain scores at different levels of target load (E). Black bars in panel D indicate discrete frequency ranges or sensors (shown in A). (**F, G**) Participants with stronger multivariate power modulation exhibit stronger drift rates for single targets (F), as well as stronger drift rate decreases under uncertainty (G). In G, dots represent linear model residuals (see methods), colored by participant. Coupled changes across target conditions are indicated by the black line. We indicate the direction of main effects for each variable via + and - (- = small decreases, -- = large decreases, + = small increases, ++ = large increases), with directions of variables on the x-axis indicated first. [*** p < .001]

Here too, we performed multiple control analyses. First, the same multivariate power-band relations noted in our task PLS model (SPMF above) were also identified in a behavioral PLS model intended to estimate optimal statistical relations between power bands and behavior (Text S4, Figure S4B). Second, while we observed increases in pre-stimulus alpha power with increasing probe uncertainty, these changes did not relate to behavioral changes or power changes during stimulus processing (Text S5, Figure S4C). Third, the entrained steady-state visual evoked potential (SSVEP) magnitude was not modulated by target load (Text S6, Figure S4D). Fourth, multivariate power changes corresponded to narrow-band, rhythm-specific indices in the theta and alpha band (Text S7, Figure S4E), and thus did not exclusively result from changes in the aperiodic background spectrum (see below).

Alpha phase modulates gamma power during sensation

Alpha rhythms have been related to phasic control over bottom-up input, as putatively encoded in gamma power (Spaak et al., 2012). To assess phase-amplitude coupling (PAC)

227　in the present data, we selected temporal alpha episodes at the single-trial level (see
228　methods, Figure 4A) and assessed the coupling between alpha phase and gamma power.
229　We observed significant alpha-gamma PAC (Figure 4B, D left), consistent with alpha-phase-
230　dependent excitability modulation. This was constrained to the occurrence of alpha episodes,
231　as no significant alpha-gamma PAC was observed prior to indicated alpha episodes (grey
232　shading in Figure 4A; Figure 4D right). Phasic gamma power modulation was observed
233　across target load levels (Figure 4F), but alpha duration decreased as a function of load
234　(Figure 4C). This suggests that alpha rhythms consistently regulated gamma power, but that
235　alpha engagement decreased as more targets became relevant.
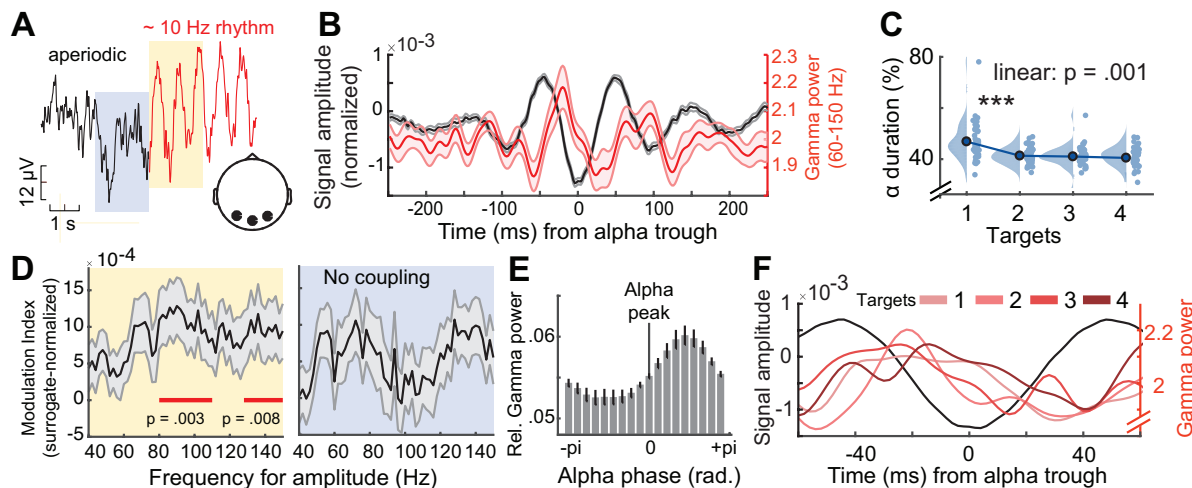

Figure 4. Alpha phase modulates gamma power during sensation. (**A**) Exemplary time series
around the onset of a detected alpha event (example from 4-target condition). Segments were pooled
across occipital channels (black dots in inset topography) and target load conditions. (**B**) Normalized
gamma power (red; mean +- SE) during alpha events (yellow shading in A), is modulated by alpha
phase (see methods). The unfiltered ERP aligned to the alpha trough is shown in black. Shaded
regions indicate standard errors. (**C**) The relative duration of alpha events decreased with increased
feature relevance. Data are individually centered across target loads. (**D**) Modulation index (MI)
indicated significant coupling between the phase of alpha and gamma power during rhythmic events
(left), but not during periods immediately prior to rhythm onset (right). MI was normalized using
surrogate data to reduce erroneous coupling (see methods). Shaded regions indicate standard errors.
(**E**) Gamma power (averaged from 60-150 Hz; mean +- SE) was maximal following alpha peaks.
Power was normalized across all phase bins (see methods). (**F**) Gamma power systematic peaks
between the peak and trough of alpha rhythms across target levels. For this analysis, alpha events
were collapsed across all participants. [*** p < .001]

Sample entropy and scale-free dynamics indicate shifts towards increased excitability

251　Next, we assessed whether reduced alpha engagement was accompanied by increases in
252　temporal irregularity, a candidate signature for system excitability (Kosciessa, Kloosterman,
253　& Garrett, 2020). We probed time-resolved fluctuations in sample entropy (SampEn), an
254　information-theoretic estimate of signal irregularity. As sample entropy is jointly sensitive to
255　broadband dynamics and narrowband rhythms, we removed the alpha frequency range using
256　band-stop-filters (8-15 Hz) to avoid contributions from alpha rhythms (see Kosciessa,
257　Kloosterman, & Garrett, 2020). A cluster-based permutation test indicated SampEn
258　increases under probe uncertainy over posterior-occipital channels (Figure 5A). Notably, the
259　magnitude of individual entropy modulation in this cluster scaled with increases in the SPMF

260 [r(137) = 0.22, 95%CI [0.05, 0.37], p = 0.01], indicating that alpha desynchronization was
261 accompanied by broadband changes in signal irregularity.
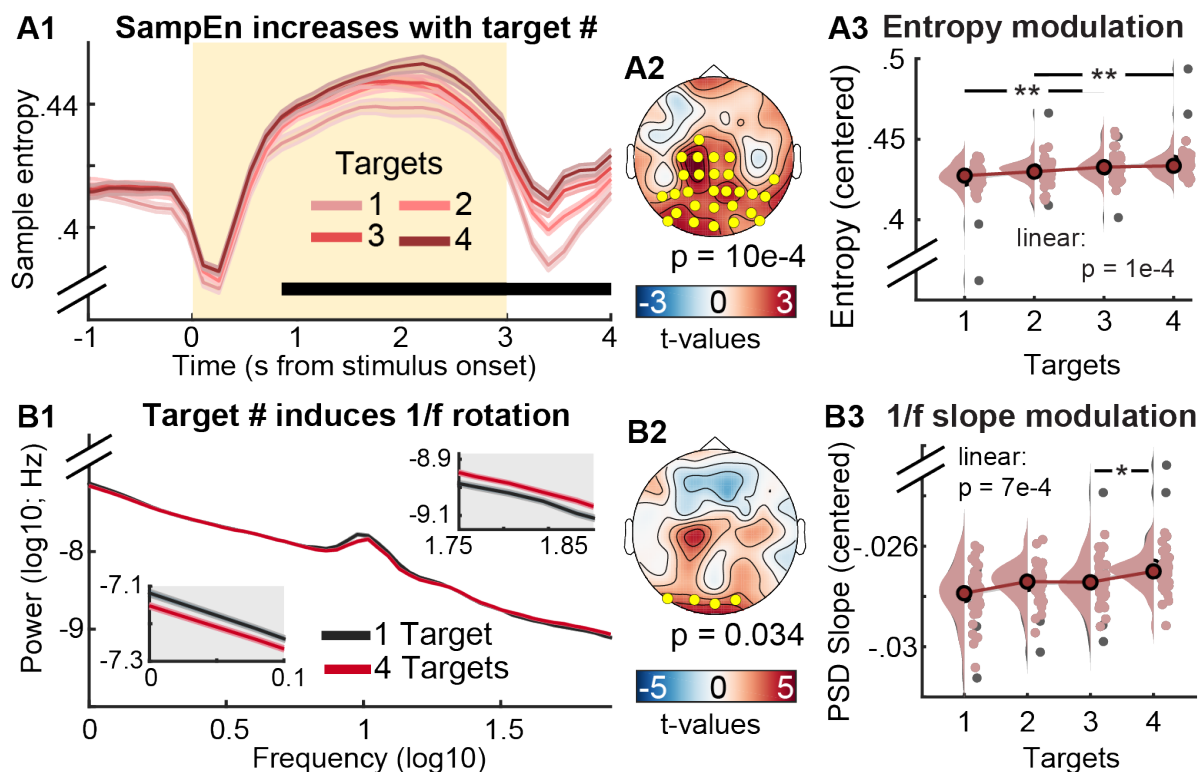
Figure 5: Uncertainty increases aperiodic dynamics during sensation as reflected in neural entropy (A) and 1/f slopes (B). (A1) Temporal traces of sample entropy (mean +- within-subject SE). The yellow background indicates the period of stimulus presentation. The black bar indicates time points at which permutation tests indicated linear load effects. (A2) Topography of linear load effect estimates, with yellow dots representing the significant cluster. (A3) Post-hoc analysis of entropy estimates within significant cluster. Grey dots indicate individual outliers (defined as Cook's distance > 2.5*mean (Cook's distance)) and have been removed from the statistical post-hoc assessment. Estimates have been within-subject centered for display purposes, while statistical analyses were run on uncentered data. (B1) Aperiodic slopes shallow with increased target load (i.e., spectral rotation across low- and high-frequencies; mean +- within-subject SE). Lower and upper insets highlight slope differences at low and high frequencies, respectively. (B2) Topography of linear load effects on 1/f slopes. Yellow dots indicate the significant occipital cluster used for post-hoc assessments. (B3) Same as A3, but for occipital aperiodic slopes. [*** p < .001, ** p < .01, * p < .05]

276 Aperiodic, scale-free spectral slopes are a major contributor to broadband SampEn, due to
277 their joint sensitivity to autocorrelative structure (Kosciessa, Kloosterman, et al., 2020), and a
278 shallowing of aperiodic (1/f) slopes has theoretically been associated with system excitability
279 (Gao et al., 2017). We therefore assessed aperiodic slope changes during the stimulus
280 period (excluding onset transients). In line with our hypothesis, participants' PSD slopes
281 shallowed under uncertainty (Figure 5B), suggesting that participants increased their
282 excitatory tone in posterior cortex. In line with the expectation that sample entropy should be
283 highly sensitive to scale-free dynamics, sample entropy was strongly related to individual
284 PSD slopes across conditions (r = .77, p <.001) and with respect to linear changes in PSD
285 slope with increasing uncertainty [r(137) = 0.44, 95%CI [0.3, 0.57], p = 4.92e-8]. In sum,
286 heightened probe uncertainty desynchronized low-frequency alpha rhythms, and elevated
287 the irregularity of cortical dynamics, in line with enhanced tonic excitability.

9

Increases in phasic pupil diameter relate to transient excitability adjustments

288 Phasic arousal changes modulate perception and local cortical excitability (for reviews see
289 Lee & Dan, 2012; McGinley, Vinck, et al., 2015). To test whether arousal increased
290 alongside uncertainty, we assessed phasic changes in pupillometric responses as a proxy for
291 arousal during stimulus presentation. We quantified phasic pupil responses via the 1st
292 temporal derivative (i.e. rate of change), as this measure has higher temporal precision and
293 has been more strongly associated with noradrenergic responses than the overall pupil
294 response (Reimer et al., 2014). Phasic pupil dilation systematically increased with probe
295 uncertainty (Figure 6). This modulation occurred on top of a general pupil constriction due to
296 stimulus-evoked changes in luminance (Figure 6A, inset), while the linear modulation
297 occurred – by stimulus design – in the absence of systematic luminance changes.


298
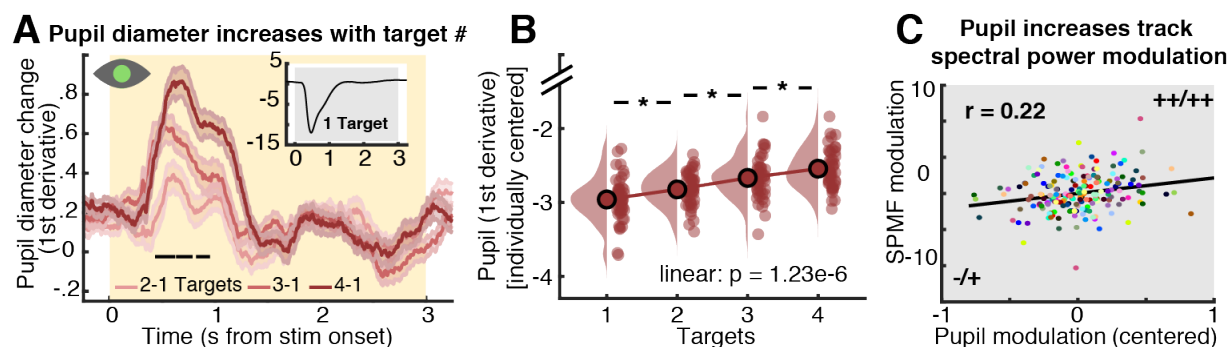
299 **Figure 6: Effect of probe uncertainty on pupil diameter as a proxy for neuromodulation. (A**)
300 Phasic changes in pupil diameter increase with number of targets (mean +- within-subject SE).
301 Significant linear load effects as indicated by a cluster-based permutation test are indicated via the
302 black line. For follow-up analyses, we extracted median pupil values from 0 to 1.5 s. For display
303 purposes but not statistics, derivative estimates were smoothed via application of a 200 ms median
304 running average. (**B**) Post-hoc analysis of load effects in extracted median values. (**C**) Coupled
305 changes between our spectral power modulation factor (SPMF) and pupil modulation. Dots represent
306 linear model residuals (see methods), colored by participant. We indicate the direction of main effects
307 for each variable via + and - (- = small decreases, -- = large decreases, + = small increases, ++ =
308 large increases). [* p < .05]

309 Next, we assessed the relation between individual modulations in pupil diameter, cortical
310 excitability and behavior. The magnitude of pupil increases tracked increases on the spectral
311 power modulation factor (SPMF) [r(137) = 0.22, 95%CI [0.06, 0.38], p = 0.01], but did not
312 directly relate to entropy [r(137) = -0.06, 95%CI [-0.23, 0.1], p = 0.45] or aperiodic slope
313 changes [r(137) = -0.04, 95%CI [-0.2, 0.13], p = 0.67]. Participants with larger increases in
314 pupil dilation also were faster integrators at baseline (r = .31, p = .033), and decreased
315 integration more so with increasing probe uncertainty [r(137) = -0.17, 95%CI [-0.33, 0], p =
316 0.05], while showing more constrained NDT increases [r(137) = -0.21, 95%CI [-0.36, -0.04], p
317 = 0.01]. This suggests that arousal jointly related to increases in local cortical excitability and
318 subsequent choices.

Thalamic BOLD modulation tracks excitability increases during sensation

319 Finally, we probed whether the thalamus acts as a subcortical nexus for sensory excitability
320 adjustments under probe uncertainty. To allow spatially resolved insights into thalamic
321 involvement, participants took part in a second, fMRI-based testing session during which

10

322 they performed the same task. First, we investigated uncertainty-related changes in BOLD
323 magnitude during stimulus processing via a task PLS. This analysis suggested two reliable
324 (LV1: permuted *p* = .001; LV2: permuted *p* = .007) latent variables (Figure 7; see Table S1
325 for peak coordinates/statistics and Figure S5A, B for complete multivariate spatial patterns
326 for the two LVs), with the first LV explaining the dominant amount of variance (89.6%
327 crossblock covariance) compared to the second LV (8.7% crossblock covariance).

328
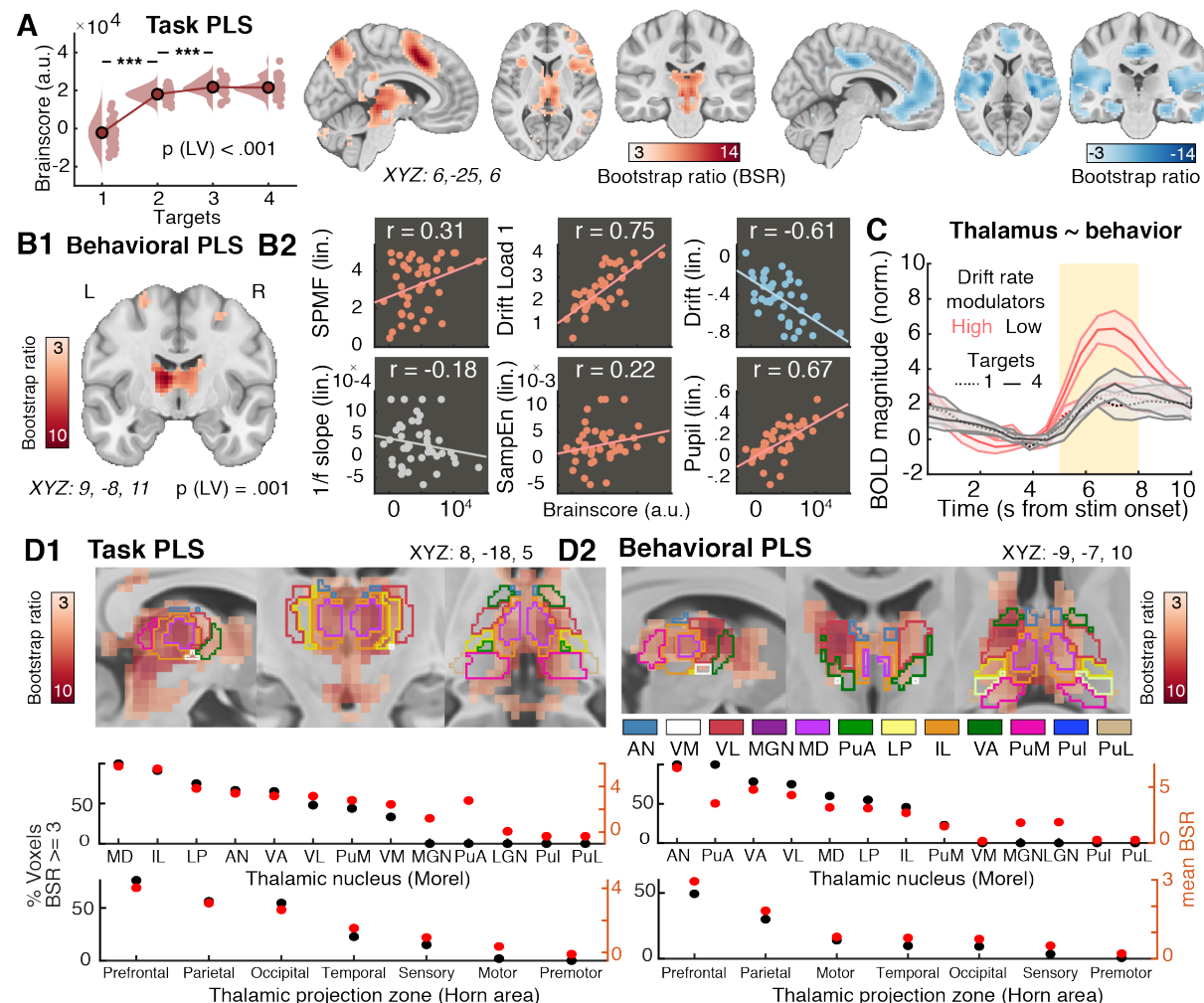
Figure 7: Upregulation of thalamic BOLD responses during stimulus processing is related to
stronger excitability increases and better performance in upcoming decision task. (**A**) Results
from multivariate task PLS investigating the relation of BOLD magnitude to attentional uncertainty.
Data are individually centered across target loads. Activity maps show positive (left) and negative
(right) bootstrap ratios of LV1, thresholded at a bootstrap ratio of 3 (p ~.001). Figure S5A presents the
full loading matrices for LV1 and LV2. (**B**) Results from behavioral PLS, probing the association
between linear changes in BOLD magnitude with behavioral, electrophysiological and pupillary
changes under uncertainty. Figure S5B presents the complete factor loadings. (**C**) Visualization of
thalamic modulation with uncertainty, split between low- and high- behavioral drift modulators (mean
+- SE). The yellow shading indicates the approximate stimulus presentation period after accounting for
the delay in the hemodynamic response function. Figure S5C plots all target conditions by group. (**D**)
Thalamic expression pattern of the first task LV (D1) and the behavioral LV (D2). Scatters below
indicate the major nuclei and projection zones in which behavioral relations are maximally reliable. For
abbreviations see methods. Strongest expression is observed in antero-medial nuclei that project to
fronto-parietal cortical targets. [*** p < .001]

11

344 The first latent variable (LV1) indicated load-related increases dominantly in cortical areas
345 encompassing the fronto-parietal and the salience network, as well as thalamus. Primary
346 positive contributors to LV1 (i.e., representing increases in BOLD with increasing probe
347 uncertainty) were located in mid-cingulate cortex (MCG), inferior parietal lobule (IPL),
348 bilateral anterior insula (aINS), inferior occipital gyrus (IOG), thalamus and bilateral inferior
349 frontal gyrus (IFG). In contrast, relative uncertainty-related decreases in BOLD magnitude
350 were dominantly observed in pallidum (potentially reflecting reduced motor preparation),
351 bilateral posterior insula (pINS), left SFG, and left mid-cingulate cortex. Individual brain score
352 increases were associated with stronger drift rate decreases [r(122) = -0.36, 95%CI [-0.5, -
353 0.19], p = 5.11e-5], but not NDT, SPMF, or entropy (all p >.05). See Text S8 for results from
354 the second latent variable (LV2), which might reflect decreased engagement at higher levels
355 of target uncertainty.

356 Finally, we performed a behavioral PLS to probe whether regional BOLD modulation tracked
357 a unified set of individual differences in the modulation of cortical excitability, arousal and
358 behavior. In fact, we observed a single significant LV (permuted *p* = .001, 46.2% crossblock
359 covariance) that dominantly loaded on anterior and midline thalamic nuclei with fronto-
360 parietal projection zones (Figure 7D), and extended broadly across almost the entirety of
361 thalamus. BOLD magnitude increases were more pronounced in participants exhibiting
362 higher drift rates (i.e., more available evidence) (r = 0.75, 95% bootstrapped (bs) CI =
363 [0.72,0.86]) and stronger drift reductions under probe uncertainty (r = -0.6, 95% bsCI = [-
364 0.78,-0.54]; Figure 7B), as well as lower baseline non-decision times (r = -.37, 95% bsCI = [-
365 .58, -.08]), confirming that increased thalamic responses reflected behaviorally adaptive
366 contextual adjustments. This association was specific to the behavioral adjustments of
367 interest, as we noted no relations with NDT modulation (r = .05, 95% bsCI = [-.31, .3]) or
368 boundary separation (r = .08, 95% CI = [-.24, .37]). Importantly, higher (dominantly thalamic)
369 BOLD modulation was further associated with greater increases on the SPMF (r = 0.31, 95%
370 CI = [0.16,0.58]), in phasic pupil dilation (r = 0.67, 95% bsCI = [0.51,0.81]) and in entropy
371 assessed during the EEG session (r = 0.22, 95% bsCI = [0.08,0.46]; Figure 7B). 1/f
372 shallowing was not stably related to BOLD modulation (r = -0.18, 95% bsCI = [-0.38,0.17]),
373 potentially due to noisier individual estimates. BOLD modulation was unrelated to
374 chronological age (r = -.19, p = .21), gender (male vs. female; r = -.27, p = .08), subjective
375 task difficulty (rated on 5-point Likert scale; r = -.02, p = .89), or framewise displacement of
376 BOLD signals (an estimate of in-scanner motion; r = -.24, p = .13). Taken together, these
377 results suggest a major role of the thalamus in integrating phasic neuromodulation to
378 regulate rhythmic and aperiodic cortical excitability according to contextual demands.

Discussion

380 To efficiently process information, cortical networks must be flexibly tuned to environmental
381 demands. Invasive studies indicate a crucial role of the thalamus in such adaptations (for a
382 review see Halassa & Kastner, 2017), but human evidence on thalamic involvement in rapid
383 cortical regime switches at the service of behavioral flexibility has been missing. By
384 combining a multi-modal experimental design with a close look at individual differences, we
385 found that processing under contextual uncertainty is associated with a triad characterized by
386 thalamic BOLD modulation, EEG-based cortical excitability, and pupil-based indicators of
387 arousal. In the light of this triad, we propose that thalamic regulation of sensory excitability is
388 crucial for adaptive sensory filtering in information-rich environments.

389   By cueing relevant dimensions of otherwise physically identical stimuli, we observed that
390   increases in the number of attentional targets reliably reduced participants' available
391   evidence (as evidenced by drift rate decreases) during subsequent perceptual decisions. We
392   interpret these changes as a negative (Dube, Emrich, & Al-Aidroos, 2017) but necessary and
393   adaptive consequence of the need to encode multiple relevant features for an eventual
394   decision regarding a single target. Concurrently, BOLD activity increased in the frontoparietal
395   network (Dosenbach et al., 2007), composed of the inferior frontal junction (Zanto, Rubens,
396   Thangavel, & Gazzaley, 2011), inferior frontal gyrus (Hampshire, Chamberlain, Monti,
397   Duncan, & Owen, 2010), and posterior parietal cortex (Weerda, Vallines, Thomas,
398   Rutschmann, & Greenlee, 2006; Wojciulik & Kanwisher, 1999), and the salience network
399   (Uddin, 2015) – including anterior insula (Nelson et al., 2010) and dorsal anterior cingulate
400   cortex (Weissman, Gopalakrishnan, Hazlett, & Woldorff, 2005). These cortical networks are
401   thought to establish the contextual relevance of environmental stimuli, and to communicate
402   this information to sensory cortex (Siegel et al., 2015). Accordingly, their BOLD activity often
403   increases alongside multifaceted demands (see above), further in line with increased
404   mediofrontal theta engagement (Cavanagh & Frank, 2014).

405   Besides such cortical responses at the group level however, we noted that individual
406   increases in cortical excitability, drift rates, and arousal were tracked primarily by the extent
407   of thalamic signal elevation, dominantly in areas with fronto-parietal projections. While past
408   work emphasized the thalamic relay of peripheral information to cortex, recent theories
409   highlight its dynamic involvement in cortical and cognitive function (for reviews see Dehghani
410   & Wimmer, 2019; Halassa & Kastner, 2017; Halassa & Sherman, 2019; Pergola et al., 2018;
411   Saalmann & Kastner, 2011; Ward, 2013; Wolff & Vann, 2019), with empirical support in
412   humans (Garrett, Epp, Perry, & Lindenberger, 2018; Hwang, Bertolero, Liu, & D'Esposito,
413   2017; Shine et al., 2019), monkeys (Fiebelkorn, Pinsk, & Kastner, 2019; Saalmann, Pinsk,
414   Wang, Li, & Kastner, 2012) and mice (Lewis et al., 2015; Schmitt et al., 2017; Wimmer et al.,
415   2015). Notably, our task responds to demands for "tasks with multifaceted cognitive
416   demands" (Pergola et al., 2018, p. 1017) to enhance sensitivity to higher-order thalamic
417   involvement. In particular, anterior and midline thalamic nuclei, in which neuro-behavioral
418   relations were maximal, may be essential for attentional set shifting (Marton, Seifikar,
419   Luongo, Lee, & Sohal, 2018; Rikhye, Gilra, & Halassa, 2018; Wright, Vann, Aggleton, &
420   Nelson, 2015) and to communicate such top-down information to sensory cortex via
421   frontoparietal network coherence (Schmitt et al., 2017). Sensory processing in turn is shaped
422   by thalamocortical transmission modes (Sherman, 2001). In 'burst mode', thalamic nuclei
423   elicit synchronous activity that can boost stimulus detection (Alitto, Rathbun, Vandeleest,
424   Alexander, & Usrey, 2019; Reinagel, Godwin, Sherman, & Koch, 1999) via non-linear gains
425   of cortical responses (G. D. Smith, Cox, Sherman, & Rinzel, 2000; Swadlow & Gusev, 2001),
426   whereas spike activity during 'tonic mode' more faithfully tracks incoming signals (Hartings,
427   Temereanca, & Simons, 2003; Sherman, 2001). Shifts from sparse bursts towards tonic
428   activity may underlie attention-related increases in thalamic BOLD magnitude observed here
429   and in previous fMRI studies (Jagtap & Diwadkar, 2016; Kim, Cilles, Johnson, & Gold, 2012;
430   Tomasi, Chang, Caparelli, & Ernst, 2007), although further work needs to elucidate the
431   relation between thalamic transmission modes and BOLD responses (but see Liu et al.,
432   2015).

433   Associated with thalamic bursting (Palva & Palva, 2007), cortical alpha rhythms may control
434   sensory gain via periodic fluctuations in excitability (Dugue, Marque, & VanRullen, 2011;
435   Haegens et al., 2011; Klimesch et al., 2007; Lorincz et al., 2009; Roux, Wibral, Singer, Aru, &

436 Uhlhaas, 2013) that can signify rapid temporal imbalances between excitation and inhibition
437 (Atallah & Scanziani, 2009; Poo & Isaacson, 2009). Supporting this notion, we observed a
438 coupling between alpha phase and high-frequency power during stimulus processing, with
439 participants engaging alpha rhythms most prevalently when prior cues afforded them a focus
440 on single stimulus features (i.e., high available sensory evidence). Alpha rhythms have been
441 consistently linked to the pulvinar nucleus (Halgren et al., 2019; Lopes da Silva, Vos,
442 Mooibroek, & Van Rotterdam, 1980; Saalmann et al., 2012; Stitt, Zhou, Radtke-Schuller, &
443 Frohlich, 2018), which also contributed to our multi-modal model. The pulvinar diffusely
444 connects to visual and fronto-parietal cortices (Arcaro, Pinsk, & Kastner, 2015), affording it to
445 build up contextual priors (Kanai, Komura, Shipp, & Friston, 2015; O'Reilly, Wyatte, &
446 Rohrlich, 2017; Rikhye, Wimmer, & Halassa, 2018) that can regulate 'bottom-up' stimulus
447 processing (Jaramillo, Mejias, & Wang, 2019), potentially via alpha rhythms (Saalmann et al.,
448 2012; Suffczynski, Kalitzin, Pfurtscheller, & da Silva, 2001). While the localization of effects
449 within the thalamus remains challenging in BOLD signals (Hwang et al., 2017), our results
450 support a perspective in which alpha rhythms – shaped via thalamocortical circuits –
451 dynamically extract relevant sensory information (Sadaghiani & Kleinschmidt, 2016) when
452 contexts afford joint distractor suppression and target enhancement (Wöstmann, Alavash, &
453 Obleser, 2019).

454 Complementing such selective gain control, overall increases in excitatory tone may serve
455 multi-feature attention when only broad attentional guidance is available. Our results provide
456 initial evidence that probe uncertainty transiently (a) desynchronizes alpha rhythms, (b)
457 increases gamma power, and (c) elevates sample entropy while shallowing spectral slopes,
458 a pattern that suggests increases in excitatory contributions to E/I mixture currents (Destexhe
459 & Rudolph, 2004; Gao et al., 2017) and asynchronous neural firing (Destexhe et al., 2003).
460 Conceptually, elevated excitability during high probe uncertainty facilitates an efficient and
461 rapid switching between parallel feature activations. In agreement with this idea, joint
462 activation of neural populations coding multiple relevant features has been observed during
463 multi-feature attention (Mo et al., 2019). Furthermore, computational modeling indicates that
464 E/I modulations in hierarchical networks optimally adjust multi-attribute choices (Pettine et
465 al., 2020). Similar to our observation of enhanced excitability during probe uncertainty,
466 Pettine et al. (2020) found increases in excitatory tone optimal for a linear weighting of
467 multiple features, whereas inhibitory engagement increased the gain for specific features
468 during more difficult perceptual decisions. As discussed above, such inhibitory tuning may
469 regulate selective target gains via alpha rhythms, in line with the presumed importance of
470 inhibitory interneurons in alpha rhythmogenesis (Lorincz et al., 2009).

471 Finally, probe uncertainty increased phasic pupil diameter, with strong links to parallel
472 adjustments in behavior, EEG-based excitability, and thalamic BOLD modulation.
473 Fluctuations in pupil diameter provide a non-invasive proxy of particularly noradrenergic drive
474 in mice (Breton-Provencher & Sur, 2019; Reimer et al., 2014; Zerbi et al., 2019), monkeys
475 (Aston-Jones & Cohen, 2005; Joshi, Li, Kalwani, & Gold, 2016) and humans (de Gee et al.,
476 2017). As such, our results support neuromodulation as a potent regulator of excitability both
477 directly at cortical targets (Constantinople & Bruno, 2011; McGinley, Vinck, et al., 2015) and
478 via thalamic circuits (Liu et al., 2015; McCormick, 1989; McCormick, McGinley, & Salkoff,
479 2015; Schiff, 2008). Functionally, pupil diameter rises during states of heightened uncertainty
480 (Krishnamurthy, Nassar, Sarode, & Gold, 2017; Nassar et al., 2012; Urai, Braun, & Donner,
481 2017), such as change points in dynamic environments (Murphy, Wilming, Hernandez-
482 Bocanegra, Prat Ortega, & Donner, 2020; Nassar et al., 2012), and multi-feature attention

483 (Alnaes et al., 2014; Koelewijn, Shinn-Cunningham, Zekveld, & Kramer, 2014), while
484 increasing alongside cortical desynchronization (Dahl, Mather, Sander, & Werkle-Bergne,
485 2020; Murphy et al., 2020; Stitt et al., 2018; Waschke, Tune, & Obleser, 2019). Our results
486 extend those observations, and suggest that neuromodulatory drive accompanies excitability
487 increases especially when contexts prevent the formation of single attentional targets,
488 potentially to serve a more faithful processing of complex environments (Berridge &
489 Waterhouse, 2003; McGinley, David, et al., 2015).

490 Multiple neuromodulators, prominently noradrenaline and acetylcholine, regulate
491 thalamocortical excitability (Lee & Dan, 2012; McCormick et al., 2015) and pupil responses
492 (Reimer et al., 2014), but may differentially serve perceptual sensitivity vs. specificity
493 demands (Shine, 2019). Specifically, noradrenergic drive may increase sensitivity to external
494 stimuli (McCormick et al., 1991; Waterhouse & Navarra, 2019) by increasing E/I ratios
495 (Froemke, Merzenich, & Schreiner, 2007; Martins & Froemke, 2015; Pfeffer et al., 2018),
496 whereas cholinergic innervation might facilitate response selectivity (Bauer et al., 2012;
497 Furey, Pietrini, & Haxby, 2000). However, as contrasting effects have also been observed for
498 these modulators (e.g., Hirata, Aguilar, & Castro-Alamancos, 2006; Minces, Pinto, Dan, &
499 Chiba, 2017; Vinck, Batista-Brito, Knoblich, & Cardin, 2015; Yu & Dayan, 2005), their
500 functional separability necessitates further work.

501 To conclude, we report initial evidence that thalamocortical excitability adjustments guide
502 human perception and decisions under uncertainty. Our results point to neuromodulatory
503 changes regulated by the thalamus that trigger behaviorally relevant switches in cortical
504 dynamics, from alpha-rhythmic gain control to increased tonic excitability, when contexts
505 require a more faithful processing of information-rich environments. Given that difficulties in
506 dealing with uncertainty, neuro-sensory hyperexcitability, and deficient E/I control are
507 hallmarks of several clinical disorders (e.g., McFadyen, Dolan, & Garrido, 2020; Yang et al.,
508 2016; Yizhar et al., 2011), we surmise that further research on individual differences in the
509 modulation of contextual excitability might advance our understanding of cognitive flexibility
510 in both healthy and diseased populations.

<div align="center">

Methods

</div>

Sample

47 healthy young adults (18-35 years, mean age = 25.8 years, SD = 4.6, 25 women) performed a dynamic visual attention task during 64-channel active scalp EEG acquisition, 42 of whom returned for a subsequent 3T fMRI session. Due to participant and scanner availability, the average span between EEG and MR testing sessions was 9.8 days (SD = 9.5 days). Participants were recruited from the participant database of the Max Planck Institute for Human Development, Berlin, Germany (MPIB). Participants were right-handed, as assessed with a modified version of the Edinburgh Handedness Inventory (Oldfield, 1971), and had normal or corrected-to-normal vision. Participants reported to be in good health with no known history of neurological or psychiatric incidences, and were paid for their participation (10 € per hour). All participants gave written informed consent according to the institutional guidelines of the Deutsche Gesellschaft für Psychologie (DGPS) ethics board, which approved the study.

Procedure: EEG Session

Participants were seated at a distance of 60 cm in front of a monitor in an acoustically and electrically shielded chamber with their heads placed on a chin rest. Following electrode placement, participants were instructed to rest with their eyes open and closed, each for 3 minutes. Afterwards, participants performed a standard Stroop task, followed by the visual attention task instruction & practice (see below), the performance of the task and a second Stroop assessment (Stroop results are not reported here). Stimuli were presented on a 60 Hz 1920x1080p LCD screen (AG Neovo X24) using PsychToolbox 3.0.11 (Brainard, 1997; Kleiner, Brainard, & Pelli, 2007; Pelli, 1997). The session lasted ~3 hours. EEG was continuously recorded from 60 active (Ag/AgCl) electrodes using BrainAmp amplifiers (Brain Products GmbH, Gilching, Germany). Scalp electrodes were arranged within an elastic cap (EASYCAP GmbH, Herrsching, Germany) according to the 10% system (Oostenveld & Praamstra, 2001), with the ground placed at AFz. To monitor eye movements, two additional electrodes were placed on the outer canthi (horizontal EOG) and one electrode below the left eye (vertical EOG). During recording, all electrodes were referenced to the right mastoid electrode, while the left mastoid electrode was recorded as an additional channel. Online, signals were digitized at a sampling rate of 1 kHz. In addition to EEG, we simultaneously tracked eye movements and assessed pupil diameter using EyeLink 1000+ hardware (SR Research, v.4.594) with a sampling rate of 1kHz.

Procedure: MRI session

Forty-two participants returned for a second testing session that included structural and functional MRI assessments. First, participants took part in a short refresh of the visual attention task ("MAAT", see below) instructions and practiced the task outside the scanner. Then, participants were located in the TimTrio 3T scanner and were instructed in the button mapping. We collected the following sequences: T1w, task (4 runs), T2w, resting state, DTI, with a 15 min out-of-scanner break following the task acquisition. The session lasted ~3 hours. Whole-brain task fMRI data (4 runs á ~11,5 mins, 1066 volumes per run) were collected via a 3T Siemens TrioTim MRI system (Erlangen, Germany) using a multi-band EPI

550 sequence (factor 4; TR = 645 ms; TE = 30 ms; flip angle 60°; FoV = 222 mm; voxel size
551 3x3x3 mm; 40 transverse slices. The first 12 volumes (12 × 645 ms = 7.7 sec) were removed
552 to ensure a steady state of tissue magnetization (total remaining volumes = 1054 per run). A
553 T1-weighted structural scan was also acquired (MPRAGE: TR = 2500 ms; TE = 4.77 ms; flip
554 angle 7°; FoV = 256 mm; voxel size 1x1x1 mm; 192 sagittal slices). A T2-weighted structural
555 scan was also acquired (GRAPPA: TR = 3200 ms; TE = 347 ms; FoV = 256 mm; voxel size
556 1x1x1 mm; 176 sagittal slices).

The multi-attribute attention task ("MAAT")

557 We designed a task to parametrically control top-down attention to multiple feature
558 dimensions, in the absence of systematic variation in bottom-up visual stimulation (see
559 Figure 1). Participants attended a dynamic square display that jointly consisted of four
560 attributes: color (red/green), movement direction (left, right), size (small, large) and saturation
561 (low, high). The task incorporates features from random dot motion tasks which have been
562 extensively studied in both animal models (Gold & Shadlen, 2007; Hanks & Summerfield,
563 2017; Siegel et al., 2015) and humans (Banca et al., 2015; Kelly & O'Connell, 2013).
564 Following the presentation of these displays, a probe queried the prevalence of one of the
565 four attributes in the display (e.g. whether the display comprised a greater proportion of
566 either smaller or larger squares). Prior to stimulus onset, valid cue presentation informed
567 participants about the active feature set, out of which one feature would be chosen as the
568 probe. We parametrically manipulated uncertainty regarding the upcoming probe by
569 systematically varying both the number and type of relevant features in the display.

570 The difficulty of each feature was determined by (a) the fundamental feature difference
571 between the two alternatives and (b) the sensory evidence for each alternative in the display.
572 For (a) the following values were used: high (RGB: 192, 255, 128) and low saturation green
573 (RGB: 255, 128, 149) and high (RGB: 128, 255, 0) and low saturated red (RGB: 255, 0, 43)
574 for color and saturation, 5 and 8 pixels for size differences and a coherence of .2 for
575 directions. For (b) the proportion of winning to losing option (i.e. sensory evidence) was
576 chosen as follows: color: 60/40; direction: 80/20; size: 65/35; luminance: 60/40. Parameter
577 difficulty was established in a pilot population, with the aim to produce above-chance
578 accuracy for individual features.

579 The experiment consisted of four runs of ~10 min, each consisting of eight blocks of eight
580 trials (i.e., a total of 32 trial blocks; 256 trials). The size and constellation of the cue set was
581 held constant within eight-trial blocks to reduce set switching and working memory demands.
582 Each trial was structured as follows: cue onset during which the relevant targets were
583 centrally presented (1 s), fixation phase (2 s), dynamic stimulus phase (3 s), probe phase
584 (incl. response; 2 s); ITI (un-jittered; 1.5 s). At the onset of each block, the valid cue
585 (attentional target set) was presented for 5 s. At the offset of each block, participants
586 received feedback for 3 s. The four attributes spanned a constellation of 16 feature
587 combinations (4x4), of which presentation frequency was matched within subjects. The size
588 and type of cue set was pseudo-randomized, such that every size and constellation of the
589 cue set was presented across blocks. Within each run of four blocks, every set size was
590 presented once, but never directly following a block of the same set size. In every block,
591 each feature in the active set acted as a probe in at least one trial. Moreover, any attribute
592 equally often served as a probe across all blocks. Winning options for each feature were
593 balanced across trials, such that (correct) button responses were equally distributed across

17

594 the experiment. To retain high motivation during the task and encourage fast and accurate
595 responses, we instructed participants that one response would randomly be drawn at the end
596 of each block; if this response was correct and faster than the mean RT during the preceding
597 block, they would earn a reward of 20 cents. However, we pseudo-randomized feedback
598 such that all participants received a fixed payout of 10 € per session. This extra money was
599 paid in addition to the participation fee at the end of the second session, at which point
600 participants were debriefed.

Behavioral estimates of probe-related decision processes

601 Sequential sampling models, such as the drift-diffusion model (DDM (Ratcliff & McKoon,
602 2008)), have been used to characterize evolving perceptual decisions in 2-alternative forced
603 choice (2AFC) random dot motion tasks (Kelly & O'Connell, 2013), where the evolving
604 decision relates to overt stimulus dynamics. In contrast with such applications, evidence
605 integration here is tied to eidetic memory traces following the probe onset, similar to
606 applications during memory retrieval (Ratcliff, 1978) or probabilistic decision making (Frank
607 et al., 2015). Here, we estimated individual evidence integration parameters within the
608 HDDM 0.6.0 toolbox (Wiecki, Sofer, & Frank, 2013) to profit from the large number of
609 participants that can establish group priors for the relatively sparse within-subject data.
610 Independent models were fit to data from the EEG and the fMRI session to allow reliability
611 assessments of individual estimates. Premature responses faster than 250 ms were
612 excluded prior to modeling, and the probability of outliers was set to 5%. 7000 Markov-Chain
613 Monte Carlo samples were sampled to estimate parameters, with the first 5000 samples
614 being discarded as burn-in to achieve convergence. We judged convergence for each model
615 by visually assessing both Markov chain convergence and posterior predictive fits. Individual
616 estimates were averaged across the remaining 2000 samples for follow-up analyses.

617 We fitted data to correct and incorrect RTs (termed 'accuracy coding' in Wiecki et al. (2013)).
618 To explain differences in decision components, we compared four separate models. In the
619 'full model', we allowed the following parameters to vary between conditions: (i) the mean
620 drift rate across trials, (ii) the threshold separation between the two decision bounds, (iii) the
621 non-decision time, which represents the summed duration of sensory encoding and response
622 execution. In the remaining models, we reduced model complexity, by only varying (a) drift,
623 (b) drift + threshold, or (c) drift + NDT, with a null model fixing all three parameters. For
624 model comparison, we first used the Deviance Information Criterion (DIC) to select the model
625 which provided the best fit to our data. The DIC compares models on the basis of the
626 maximal log-likelihood value, while penalizing model complexity. The full model provided the
627 best fit to the empirical data based on the DIC index (Figure S1B) in both the EEG and the
628 fMRI session. However, this model indicated an increase in decision thresholds (i.e.,
629 boundary separation) without an equivalent in the electrophysiological data (Figure S1C). We
630 therefore fixed the threshold parameter across conditions, in line with previous work
631 constraining model parameters on the basis of electrophysiological evidence (McGovern et
632 al., 2018).

EEG preprocessing

633 Preprocessing and analysis of EEG data were conducted with the FieldTrip toolbox
634 (Oostenveld, Fries, Maris, & Schoffelen, 2011) and using custom-written MATLAB (The
635 MathWorks Inc., Natick, MA, USA) code. Offline, EEG data were filtered using a 4th order

18

636 Butterworth filter with a pass-band of 0.5 to 100 Hz. Subsequently, data were down-sampled
637 to 500 Hz and all channels were re-referenced to mathematically averaged mastoids. Blink,
638 movement and heart-beat artifacts were identified using Independent Component Analysis
639 (ICA; Bell & Sejnowski, 1995) and removed from the signal. Artifact-contaminated channels
640 (determined across epochs) were automatically detected using (a) the FASTER algorithm
641 (Nolan, Whelan, & Reilly, 2010), and by (b) detecting outliers exceeding three standard
642 deviations of the kurtosis of the distribution of power values in each epoch within low (0.2-2
643 Hz) or high (30-100 Hz) frequency bands, respectively. Rejected channels were interpolated
644 using spherical splines (Perrin, Pernier, Bertrand, & Echallier, 1989). Subsequently, noisy
645 epochs were likewise excluded based on FASTER and on recursive outlier detection. Finally,
646 recordings were segmented to participant cues to open their eyes, and were epoched into
647 non-overlapping 3 second pseudo-trials. To enhance spatial specificity, scalp current density
648 estimates were derived via 4th order spherical splines (Perrin et al., 1989) using a standard
649 1005 channel layout (conductivity: 0.33 S/m; regularization: 1^{-05}; 14th degree polynomials).

Electrophysiological estimates of probe-related decision processes

650 **Centroparietal Positive Potential (CPP).** The centroparietal positive potential (CPP) is an
651 electrophysiological signature of internal evidence-to-bound accumulation (Kelly & O'Connell,
652 2013; McGovern et al., 2018; O'Connell et al., 2012). We probed the task modulation of this
653 established signature and assessed its convergence with behavioral parameter estimates.
654 To derive the CPP, preprocessed EEG data were low-pass filtered at 8 Hz with a 6th order
655 Butterworth filter to exclude low-frequency oscillations, epoched relative to response and
656 averaged across trials within each condition. In accordance with the literature, this revealed a
657 dipolar scalp potential that exhibited a positive peak over parietal channel POz (see Figure
658 2). We temporally normalized individual CPP estimates to a condition-specific baseline
659 during the final 250 ms preceding probe onset. As a proxy of evidence drift rate, CPP slopes
660 were estimates via linear regression from -250 ms to -100 ms surrounding response
661 execution, while the average CPP amplitude from -50 ms to 50 ms served as an indicator of
662 decision thresholds (i.e., boundary separation) (e.g., McGovern et al., 2018).

663 To investigate whether a similar 'ramping' potential was observed during stimulus
664 presentation, we aligned data to stimulus onset and temporally normalized signals to the
665 condition-specific signal during the final 250 ms prior to stimulus onset. During stimulus
666 presentation, no 'ramp'-like signal or load modulation was observed at the peak CPP
667 channel. This suggests that immediate choice requirements were necessary for the
668 emergence of the CPP, although prior work has shown the CPP to be independent of explicit
669 motor requirements (O'Connell et al., 2012).

670 Finally, we assessed whether differences between probed stimulus attributes could account
671 for load-related CPP changes (Figure S2C). For this analysis, we selected trials separately
672 by condition and probed attribute. Note that for different probes, but not cues, trials were
673 uniquely associated with each feature and trial counts were approximately matched across
674 conditions. We explored differences between different conditions via paired t-tests. To
675 assess load effects on CPP slopes and thresholds as a function of probed attribute, we
676 calculated 1st-level load effects by means of a linear model, and assessed their difference
677 from zero via paired t-tests.

Contralateral mu-beta. Decreases in contralateral mu-beta power provide a complementary, effector-specific signature of evidence integration (Donner et al., 2009; McGovern et al., 2018). We estimated mu-beta power using 7-cycle wavelets for the 8-25 Hz range with a step size of 50 ms. Spectral power was time-locked to probe presentation and response execution. We re-mapped channels to describe data recorded contra- and ipsi-lateral to the executed motor response in each trial, and averaged data from those channels to derive grand average mu-beta time courses. Individual average mu-beta time series were baseline-corrected using the -400 to -200 ms prior to probe onset, separately for each condition. For contralateral motor responses, remapped sites C3/5 and CP3/CP5 were selected based on the grand average topography for lateralized response executions (see inset in Figure S2A). As a proxy of evidence drift rate, mu-beta slopes were estimates via linear regression from -250 ms to -50 ms prior to response execution, while the average power -50 ms to 50 ms served as an indicator of decision thresholds (e.g., McGovern et al., 2018).

Electrophysiological indices of top-down modulation during sensation

Low-frequency alpha and theta power. We estimated low-frequency power via a 7-cycle wavelet transform, using, for linearly spaced center frequencies in 1 Hz steps from 2 to 15 Hz. The step size of estimates was 50 ms, ranging from -1.5 s prior to cue onset to 3.5 s following stimulus offset. Estimates were log10-transformed at the single trial level (Smulders, ten Oever, Donkers, Quaedflieg, & van de Ven, 2018), with no explicit baseline.

High-frequency gamma power. Gamma responses were estimated using multi-tapers (five tapers; discrete prolate spheroidal sequences) with a step size of 200 ms, a window length of 400 ms and a frequency resolution of 2.5 Hz. The frequency range covered frequencies between 45-90 Hz, with spectral smoothing of 8 Hz. Estimates were log10-transformed at the single trial level. We normalized individual gamma-band responses via single-trial z-normalization. In particular, for each frequency, we subtracted single-trial power -700 to -100 ms prior to stimulus onset, and divided by the standard deviation of power values during the same period. Finally, to account for baseline shifts during the pre-stimulus period, we subtracted condition-wise averages during the same baseline period.

Multivariate assessment of spectral power changes with stimulus onset and uncertainty. To determine changes in spectral power upon stimulus onset, and during stimulus presentation with load, we entered individual power values into multivariate partial least squares (PLS) analyses (see *Multivariate partial least squares analyses*) using the MEG-PLS toolbox [version 2.02b] (Cheung, Kovacevic, Fatima, Misic, & McIntosh, 2016). We concatenated low- (2-15 Hz) and high-frequency (45-90 Hz) power matrices to assess joint changes in the PLS models. To examine a multivariate contrast of spectral changes upon stimulus onset (averaged across conditions) with spectral power in the pre-stimulus baseline period, we performed a task PLS on data ranging from 500 ms pre-stim to 500 ms post-stim. Temporal averages from -700 to -100 ms pre-stimulus onset were subtracted as a baseline. To assess power changes as a function of probe uncertainty, we segmented the data from 500 ms post stim onset to stimulus offset (to exclude transient evoked onset responses), and calculated a task PLS concerning the relation between experimental uncertainty conditions and time-space-frequency power values. As a control, we performed a behavioral PLS analysis to assess the relevance of individual frequency contributions to the behavioral relation. For this analysis, we computed linear slopes (target amount) for each

20

722 time-frequency point at the 1st (within-subject) level, which were subsequently entered into
723 the 2nd level PLS analysis. On the behavioral side, we assessed both linear changes in pupil
724 diameter, as well as drift rates during selective attention and linear decreases in drift rate
725 under uncertainty. Finally, spontaneous fluctuations in pre-stimulus power have been linked
726 to fluctuations in cortical excitability (Iemi, Chaumon, Crouzet, & Busch, 2017; Lange,
727 Oostenveld, & Fries, 2013). We thus probed the role of upcoming processing requirements
728 on pre-stimulus oscillations, as well as the potential relation to behavioral outcomes using
729 task and behavioral PLS analyses. The analysis was performed as described above, but
730 restricted to time points occurring during the final second prior to stimulus onset.

731 **Steady State Visual Evoked Potential (SSVEP).** The SSVEP characterizes the phase-
732 locked, entrained visual activity (here 30 Hz) during dynamic stimulus updates (e.g., Ding,
733 Sperling, & Srinivasan, 2006). These features differentiate it from induced broadband activity
734 or muscle artefacts in similar frequency bands. We used these properties to normalize
735 individual single-trial SSVEP responses prior to averaging: (a) we calculated an FFT for
736 overlapping one second epochs with a step size of 100 ms (Hanning-based multitaper),
737 averaged them within each load condition and, (b) spectrally normalized 30 Hz estimates by
738 subtracting the average of estimates at 28 and 32 Hz, effectively removing broadband effects
739 (i.e., aperiodic slopes), (c) and finally, we subtracted a temporal baseline -700 to -100 ms
740 prior to stimulus onset. Linear load effects on SSVEPs were assessed by univariate cluster-
741 based permutation tests on channel x time data (see *Univariate statistical analyses using*
742 *cluster-based permutation tests*).

743 **Time-resolved sample entropy.** Sample entropy (Richman & Moorman, 2000) quantifies
744 the irregularity of a time series of length *N* by assessing the conditional probability that two
745 sequences of *m* consecutive data points will remain similar when another sample (*m+1*) is
746 included in the sequence (for a visual example see Figure 1A). Sample entropy is defined as
747 the inverse natural logarithm of this conditional similarity: $\mathrm{SampEn}(m, r, N) =$
748 $-\log\left(\frac{p^{m+1}(r)}{p^m(r)}\right)$. The similarity criterion (*r*) defines the tolerance within which two points are
749 considered similar and is defined relative to the standard deviation (~variance) of the signal
750 (here set to r = .5). We set the sequence length *m* to 2, in line with previous applications
751 (Kosciessa, Kloosterman, et al., 2020). An adapted version of sample entropy calculations
752 was used (Grandy, Garrett, Schmiedek, & Werkle-Bergner, 2016; Kloosterman, Kosciessa,
753 Lindenberger, Fahrenfort, & Garrett, 2019; Kosciessa, Kloosterman, et al., 2020), wherein
754 entropy is estimated across discontinuous data segments to provide time-resolved estimates.
755 The estimation of scale-wise entropy across trials allows for an estimation of coarse scale
756 entropy also for short time-bins, i.e., without requiring long, continuous signals, while quickly
757 converging with entropy estimates from continuous recordings (Grandy et al., 2016). To
758 remove the influence of posterior-occipital low-frequency rhythms on entropy estimates, we
759 notch-filtered the 8-15 Hz alpha band using 6th order Butterworth filter prior to the entropy
760 calculation (Kosciessa, Kloosterman, et al., 2020). Time-resolved entropy estimates were
761 calculated for 500 ms windows from -1 s pre-stimulus to 1.25 s post-probe with a step size of
762 150 ms. As entropy values are implicitly normalized by the variance in each time bin via the
763 similarity criterion, no temporal baselining was used. Linear load effects on entropy were
764 assessed by univariate cluster-based permutation tests on channel x time data (see
765 *Univariate statistical analyses using cluster-based permutation tests*).

766 **Aperiodic (1/f) slopes.** The aperiodic 1/f slope of neural recordings is closely related to the
767 sample entropy of broadband signals (Kosciessa, Kloosterman, et al., 2020), and has been

21

768 suggested as a proxy for 'cortical excitability' and excitation-inhibition balance (Gao et al.,
769 2017). Spectral estimates were computed by means of a Fast Fourier Transform (FFT) over
770 the final 2.5 s of the presentation period (to exclude onset transients) for 41 logarithmically
771 spaced frequencies between 2 and 64 Hz (Hanning-tapered segments zero-padded to 10 s)
772 and subsequently averaged. Spectral power was log10-transformed to render power values
773 more normally distributed across subjects. Power spectral density (PSD) slopes were derived
774 by linearly regressing log-transformed power values on log-transformed frequencies. The
775 spectral range from 7-13 Hz was excluded from the background fit to exclude a bias by the
776 narrowband alpha peak (Kosciessa, Kloosterman, et al., 2020) and thus to increase the
777 specificity to aperiodic variance. Linear load effects on 1/f slopes were assessed by
778 univariate cluster-based permutation tests on channel data (see *Univariate statistical*
779 *analyses using cluster-based permutation tests*).

780 **Rhythm-specific estimates.** Spectral power estimates conflate rhythmicity with aperiodic
781 events in time, space and magnitude (Kosciessa, Grandy, Garrett, & Werkle-Bergner, 2020).
782 Given that we observed changes in aperiodic slopes, we verified that observed narrowband
783 effects in the theta and alpha band describe narrowband changes in rhythmicity. For this
784 purpose, we identified single-trial spectral events using the extended BOSC method (Caplan,
785 Madsen, Raghavachari, & Kahana, 2001; Kosciessa, Grandy, et al., 2020; Whitten, Hughes,
786 Dickson, & Caplan, 2011). In short, this method identifies stereotypic 'rhythmic' events at the
787 single-trial level, with the assumption that such events have significantly higher power than
788 the 1/f background and occur for a minimum number of cycles at a particular frequency. This
789 procedure dissociates narrowband spectral peaks from the aperiodic background spectrum.
790 Here, we used a three-cycle threshold during detection, while defining the power threshold
791 as the 95th percentile above the individual background power. A 5-cycle wavelet was used to
792 provide the time-frequency transformations for 49 logarithmically-spaced center frequencies
793 between 1 and 64 Hz. Rhythmic episodes were detected as described in (Kosciessa,
794 Grandy, et al., 2020). Prior to fitting the 1/f slopes, the most dominant individual rhythmic
795 alpha peak between 8 and 15 Hz was removed, as well as the 28-32 Hz range, to exclude
796 the SSVEP. Detection of episodes was restricted to the time of stimulus presentation,
797 excluding the first 500 ms to reduce residual pre-stimulus activity and onset transients.
798 Within each participant and channel, the duration and SNR of individual episodes with a
799 mean frequency between 4-8 Hz (Theta) and 8-15 Hz (Alpha) were averaged across trials.
800 Effects of target number were assessed within the averaged spatial clusters indicated in
801 Figure 3 by means of paired t-tests.

Alpha-gamma phase-amplitude coupling (PAC)

802 We assessed alpha-phase-to-gamma-amplitude coupling to assess the extent of phasic
803 modulation of gamma power within the alpha band. As phase information is only
804 interpretable during the presence of a narrowband rhythm (Aru et al., 2015), we focused our
805 main analysis on 250 ms time segments following the estimated onset of a rhythm in the 8-
806 15 Hz alpha range (see *Rhythm-specific estimates* above; Figure 4A). This time window
807 ensured that segments fulfilled the 3-cycle criterion imposed during eBOSC rhythm detection
808 to ensure that a rhythm was present. We selected three occipital channels with maximal
809 gamma power (O1, O2, Oz; shown in Figure 4A) and pooled detected alpha episodes across
810 these channels. We pooled data across load conditions, as we observed no consistent PAC
811 within individual load conditions (data not shown), perhaps due to low episode counts. To
812 derive the alpha carrier phase, we band-pass filtered signals in the 8-15 Hz band, and

22

813   estimated the analytic phase time series via Hilbert transform. For the amplitude of
814   modulated frequencies, we equally applied band-pass filters from 40 to 150 Hz (step size: 2
815   Hz), with adaptive bandwidths (+/- 20% of center frequency). Filtering was implemented
816   using MATLAB's acausal filtfilt() routine using linear finite impulse response (FIR) filters with
817   an adaptive filter order set as 3 times the ratio of the sampling frequency to the low-
818   frequency cutoff (Tort et al., 2008). For each applied bandpass filter, we removed 250 ms at
819   each edge to avoid filter artifacts. For each frequency, narrowband signals were z-scored to
820   normalize amplitudes across frequencies, and absolute values of the Hilbert-derived complex
821   signal were squared to produce instantaneous power time series. We estimated the MI
822   between the 8-15 Hz phase and high-frequency power via normalized entropy (Tort et al.,
823   2008) using 16 phase bins. Power estimates were normalized by dividing the bin-specific
824   power by the sum of power across bins. To make MI estimates robust against random
825   coupling, we estimated MI for 1000 surrogate data, which shuffled the trial association of
826   phase and amplitude information. We subtracted the mean surrogate MI value from the
827   original MI index for a final, surrogate-normalized MI estimate. The resulting MI estimates
828   across frequencies were then subjected to a cluster-based permutation test to assess
829   significant clusters from zero using paired t-tests. For Figure 4B, we followed the procedure
830   by Canolty et al. (2006). Alpha troughs were identified as local minima of phases < [-pi+.01].
831   For visualization, data were averaged across center frequencies from 80-150 Hz, as
832   significant coupling overlapped with this range. We performed identical analyses for the 250
833   ms periods prior to rhythm onset (grey shading in Figure 4A) as a control condition. We
834   performed analogous phase-amplitude-coupling analyses for the Mean Vector Length (MVL;
835   Canolty et al., 2006) index, with comparable results (data not shown).

Analyses of pupil diameter

836   Pupil diameter was recorded during the EEG session using EyeLink 1000 at a sampling rate
837   of 1000 Hz, and was analyzed using FieldTrip and custom-written MATLAB scripts. Blinks
838   were automatically indicated by the EyeLink software (version 4.40). To increase the
839   sensitivity to periods of partially occluded pupils or eye movements, the first derivative of
840   eye-tracker-based vertical eye movements was calculated, z-standardized and outliers >= 3
841   STD were removed. We additionally removed data within 150 ms preceding or following
842   indicated outliers. Finally, missing data were linearly interpolated and data were epoched to
843   3.5 s prior to stimulus onset to 1 s following stimulus offset. We quantified phasic arousal
844   responses via the 1st temporal derivative (i.e. rate of change) of pupil diameter traces, as this
845   measure (i) has higher temporal precision and (ii) has been more strongly associated with
846   noradrenergic responses than the overall response (Reimer et al., 2014). We downsampled
847   pupil time series to 200 Hz. For visualization, but not statistics, we smoothed pupil traces
848   using a moving average median of 200 ms. We statistically assessed a linear load effect
849   using a cluster-based permutation test on the 1D pupil traces (see *Univariate statistical*
850   *analyses using cluster-based permutation tests*). For post-hoc assessments, we extracted
851   the median pupil derivative during the first 1.5 s following stimulus onset.

fMRI-based analyses

852   **Preprocessing of functional MRI data.** fMRI data were preprocessed with FSL 5
853   (RRID:SCR_002823) (Jenkinson, Beckmann, Behrens, Woolrich, & Smith, 2012; S. M. Smith
854   et al., 2004). Pre-processing included motion correction using McFLIRT, smoothing (7mm)

855 and high-pass filtering (.01 Hz) using an 8th order zero-phase Butterworth filter applied using
856 MATLAB's filtfilt function. We registered individual functional runs to the individual, ANTs
857 brain-extracted T2w images (6 DOF), to T1w images (6 DOF) and finally to 3mm standard
858 space (ICBM 2009c MNI152 nonlinear symmetric) (Fonov et al., 2011) using nonlinear
859 transformations in ANTs (Avants et al., 2011). (For one participant, no T2w image was
860 acquired and 6 DOF transformation of BOLD data was preformed directly to the T1w
861 structural scan.) We then masked the functional data with the ICBM 2009c GM tissue prior
862 (thresholded at a probability of 0.25), and detrended the functional images (up to a cubic
863 trend) using SPM8.

864 We also used a series of extended preprocessing steps to further reduce potential non-
865 neural artifacts (Garrett, Kovacevic, McIntosh, & Grady, 2010; Garrett et al., 2015).
866 Specifically, we examined data within-subject, within-run via spatial independent component
867 analysis (ICA) as implemented in FSL-MELODIC (Beckmann & Smith, 2004). Due to the high
868 multiband data dimensionality in the absence of low-pass filtering, we constrained the
869 solution to 30 components per participant. Noise components were identified according to
870 several key criteria: a) Spiking (components dominated by abrupt time series spikes);
871 b) Motion (prominent edge or "ringing" effects, sometimes [but not always] accompanied by
872 large time series spikes); c) Susceptibility and flow artifacts (prominent air-tissue boundary or
873 sinus activation; typically represents cardio/respiratory effects); d) White matter (WM) and
874 ventricle activation (Birn, 2012); e) Low-frequency signal drift (A. M. Smith et al., 1999); f)
875 High power in high-frequency ranges unlikely to represent neural activity (≥ 75% of total
876 spectral power present above .10 Hz;); and g) Spatial distribution ("spotty" or "speckled"
877 spatial pattern that appears scattered randomly across ≥ 25% of the brain, with few if any
878 clusters with ≥ 80 contiguous voxels [at 2x2x2 mm voxel size]). Examples of these various
879 components we typically deem to be noise can be found in (Garrett, McIntosh, & Grady,
880 2014). By default, we utilized a conservative set of rejection criteria; if manual classification
881 decisions were challenging due to mixing of "signal" and "noise" in a single component, we
882 generally elected to keep such components. Three independent raters of noise components
883 were utilized; > 90% inter-rater reliability was required on separate data before denoising
884 decisions were made on the current data. Components identified as artifacts were then
885 regressed from corresponding fMRI runs using the regfilt command in FSL.

886 To reduce the influence of motion and physiological fluctuations, we regressed FSL's 6 DOF
887 motion parameters from the data, in addition to average signal within white matter and CSF
888 masks. Masks were created using 95% tissue probability thresholds to create conservative
889 masks. Data and regressors were demeaned and linearly detrended prior to multiple linear
890 regression for each run. To further reduce the impact of potential motion outliers, we
891 censored significant DVARS outliers during the regression as described by (Power et al.,
892 2014). In particular, we calculated the 'practical significance' of DVARS estimates and
893 applied a threshold of 5 (Afyouni & Nichols, 2018). The regression-based residuals were
894 subsequently spectrally interpolated during DVARS outliers as described in (Power et al.,
895 2014) and (Parkes, Fulcher, Yucel, & Fornito, 2018). BOLD analyses were restricted to
896 participants with both EEG and MRI data available (N = 42).

897 **1st level analysis: univariate beta weights for load conditions.** We conducted a 1st level
898 analysis using SPM12 to identify beta weights for each load condition separately. Design
899 variables included stimulus presentation by load (4 volumes; parametrically modulated by
900 sequence position), onset cue (no mod.), probe (2 volumes, parametric modulation by RT).

24

901 Design variables were convolved with a canonical HRF, including its temporal derivative as a
902 nuisance term. Nuisance regressors included 24 motion parameters (Friston, Williams,
903 Howard, Frackowiak, & Turner, 1996), as well as continuous DVARS estimates.
904 Autoregressive modelling was implemented via FAST. Output beta images for each load
905 condition were finally averaged across runs.

906 **2nd level analysis: Multivariate modulation of BOLD responses.** We investigated the
907 multivariate modulation of the BOLD response at the 2nd level using PLS analyses (see
908 *Multivariate partial least squares analyses*). Specifically, we probed the relationship between
909 voxel-wise 1st level beta weights and probe uncertainty within a task PLS. Next, we assessed
910 the relationship between task-related BOLD signal changes and interindividual differences in
911 the joint modulation of decision processes, cortical excitability, and pupil modulation by
912 means of a behavioral PLS. For this, we first calculated linear slope coefficients for voxel-
913 wise beta estimates. Then, we included behavioral variables including HDDM parameter
914 estimates during selective attention, as well as linear changes with load, individual linear
915 condition modulation of the following variables: multivariate spectral power, pupil dilation, 1/f
916 modulation and entropy residuals. Prior to these covariates in the model, we visually
917 assessed whether the distribution of linear changes variables was approximately Gaussian.
918 In the case of outliers (as observed for the SPMF, 1/f slopes, and entropy), we winsorized
919 values at the 95th percentile. For visualization, spatial clusters were defined based on a
920 minimum distance of 10 mm, and by exceeding a size of 25 voxels. We identified regions
921 associated with peak activity based on cytoarchitectonic probabilistic maps implemented in
922 the SPM Anatomy Toolbox (Version 2.2c) (Eickhoff et al., 2005). If no assignment was found,
923 the most proximal assignment to the coordinates reported in Table S1 within the cluster was
924 reported.

925 **Temporal dynamics of thalamic engagement.** To visualize the modulation of thalamic
926 activity by load, we extracted signals within a binary thalamic mask extracted from the Morel
927 atlas, including all subdivisions. Preprocessed BOLD timeseries were segmented into trials,
928 spanning the period from the stimulus onset to the onset of the feedback phase. Given a
929 time-to-peak of a canonical hemodynamic response function (HRF) between 5-6 seconds,
930 we designated the 3 second interval from 5-8 seconds following the stimulus onset trigger as
931 the stimulus presentation interval, and the 2 second interval from 3-5 s as the fixation
932 interval, respectively. Single-trial time series were then temporally normalized to the temporal
933 average during the approximate fixation interval. To visualize inter-individual differences in
934 thalamic engagement, we performed a median split across participants based on their
935 individual drift modulation.

936 **Thalamic loci of behavioral PLS.** To assess the thalamic loci of most reliable behavioral
937 relations (Figure S5C), we assessed bootstrap ratios within two thalamic masks. First, for
938 nucleic subdivisions, we used the Morel parcellation scheme as consolidated and kindly
939 provided by (Hwang et al., 2017) for 3 mm data at 3T field strength. The abbreviations are as
940 follows: AN: anterior nucleus; VM: ventromedial; VL: ventrolateral; MGN: medial geniculate
941 nucleus; LGN: lateral geniculate nucleus; MD: mediodorsal; PuA: anterior pulvinar; LP:
942 lateral-posterior; IL: intra-laminar; VA: ventral-anterior; PuM: medial pulvinar; Pul: pulvinar
943 proper; PuL: lateral pulvinar. Second, to assess cortical white-matter projections we
944 considered the overlap with seven structurally-derived cortical projection zones suggested
945 by (Horn & Blankenburg, 2016), which were derived from a large adult sample ($N = 169$). We

946 binarized continuous probability maps at a relative 75% threshold of the respective maximum
947 probability, and re-sliced masks to 3 mm size.

Statistical analyses

948 **Assessment of covarying load effect magnitudes between measures.** To assess a linear
949 modulation of dependent variables, we calculated 1st level beta estimates for the effect of
950 load (y = intercept+β*LOAD+e) and assessed the slope difference from zero at the group
951 level using paired t-tests. We assessed the relation of individual load effects between
952 measures of interest by means of partial repeated measures correlations. In a simplified
953 form, repeated measured correlation (Bakdash & Marusich, 2017) fits a linear model
954 between two variables x1 and x2 of interest, while controlling for repeated assessments
955 within subjects [x1~1+β1*ID+β2*x2+e] (1). Crucially, to exclude bivariate relations that
956 exclusively arise from joint main effects of number of targets, we added target load as an
957 additional categorical covariate [x1~1+β1*ID+β2*LOAD+β3*x2+e] (2) to remove group
958 condition means. Resulting estimates characterize the group-wise coupling in the (zero-
959 centered) magnitude of changes between the DV and the IV across the four load levels. To
960 identify the directionality of the coupling, we assessed the direction of main effects for x1 and
961 x2. We statistically compared this model to a null model without the term of interest
962 [x1~1+β1*ID+β2*LOAD +e] (3) to assess statistical significance. We report the bivariate
963 residual effect size by assessing the square root of partial eta squared. We extend this model
964 with additional beta*covariate terms when reporting control for additional covariates.

965 **Within-subject centering.** To better visualize effects within participants, we use within-
966 subject centering across repeated measures conditions by subtracting individual condition
967 means, and adding global means. For these visualizations, only the mean of the dependent
968 values is directly informative, as the plotted spread reflects within-subject, and not between-
969 subject, variation. This procedure is similar to the creation of within-subject standard errors.
970 Within-subject centering is exclusively used for display, but not statistical calculations.

971 **Univariate cluster-based permutation analyses.** For data with a low-dimensional structure
972 (e.g., based on a priori averaging or spatial cluster assumptions), we used univariate cluster-
973 based permutation analyses (CBPAs) to assess significant modulations by target load or with
974 stimulus onset. These univariate tests were performed by means of dependent samples t-
975 tests; cluster-based permutation tests (Maris & Oostenveld, 2007) were performed to control
976 for multiple comparisons. Initially, a clustering algorithm formed clusters based on significant
977 t-tests of individual data points (p <.05, two-sided; cluster entry threshold) with the spatial
978 constraint of a cluster covering a minimum of three neighboring channels. Then, the
979 significance of the observed cluster-level statistic, based on the summed t-values within the
980 cluster, was assessed by comparison to the distribution of all permutation-based cluster-level
981 statistics. The final cluster p-value that we report in all figures was assessed as the
982 proportion of 1000 Monte Carlo iterations in which the cluster-level statistic was exceeded.
983 Cluster significance was indicated by p-values below .025 (two-sided cluster significance
984 threshold).

985 **Multivariate partial least squares analyses.** For data with a high-dimensional structure, we
986 performed multivariate partial least squares analyses (Krishnan, Williams, McIntosh, & Abdi,
987 2011; McIntosh, Bookstein, Haxby, & Grady, 1996; McIntosh & Lobaugh, 2004). To assess

26

988 main effect of probe uncertainty or stimulus onset, we performed Task PLS analyses. Task
989 PLS begins by calculating a between-subject covariance matrix (COV) between conditions
990 and each neural value (e.g., time-space-frequency power), which is then decomposed using
991 singular value decomposition (SVD). This yields a left singular vector of experimental
992 condition weights (U), a right singular vector of brain weights (V), and a diagonal matrix of
993 singular values (S). Task PLS produces orthogonal latent variables (LVs) that reflect optimal
994 relations between experimental conditions and the neural data. To examine multivariate
995 relations between neural data and other variables of interest, we performed behavioral PLS
996 analyses. This analysis initially calculates a between-subject correlation matrix (CORR)
997 between (1) each brain index of interest (e.g., spectral power, 1st level BOLD beta values)
998 and (2) a second 'behavioral' variable of interest (note that although called behavioral, this
999 variable can reflect any variable of interest, e.g., behavior, pupil dilation, spectral power).
1000 CORR is then decomposed using singular value decomposition (SVD): $SVD_{CORR} = USV´$,
1001 which produces a matrix of left singular vectors of cognition weights (U), a matrix of right
1002 singular vectors of brain weights (V), and a diagonal matrix of singular values (S). For each
1003 LV (ordered strongest to weakest in S), a data pattern results which depicts the strongest
1004 available relation to the variable of interest. Significance of detected relations of both PLS
1005 model types was assessed using 1000 permutation tests of the singular value corresponding
1006 to the LV. A subsequent bootstrapping procedure indicated the robustness of within-LV
1007 neural saliences across 1000 resamples of the data (Efron & Tibshirani, 1986). By dividing
1008 each brain weight (from V) by its bootstrapped standard error, we obtained "bootstrap ratios"
1009 (BSRs) as normalized robustness estimates. We generally thresholded BSRs at values of
1010 ±3.00 (~99.9% confidence interval). We also obtained a summary measure of each
1011 participant's robust expression of a particular LV's pattern (a within-person "brain score") by
1012 either (1) multiplying the vector of brain weights (V) from each LV by within-subject vectors of
1013 the neural values (separately for each condition within person) for the Task PLS models, or
1014 (2) in the behavioral PLS model, by multiplying the model-based vector of weights (V) by
1015 each participant's vector of neural values (P), producing a single within-subject value: Brain
1016 score = $VP´$.

Acknowledgements

Funding

1029   centre.mpg.de/en/comp2psych. The funders had no role in study design, data collection and
1030   analysis, decision to publish, or preparation of the manuscript.

Declaration of Interests

1031   The authors declare no competing interests.

Author contributions

1032   JQK: Conceptualization, Methodology, Investigation, Software, Formal analysis,
1033   Visualization, Writing – original draft, Writing – review and editing, Validation, Data Curation;
1034   UL: Conceptualization, Resources, Writing – review and editing, Supervision, Funding
1035   acquisition; DDG: Conceptualization, Methodology, Software, Resources, Writing—review
1036   and editing, Supervision, Project administration, Funding acquisition.

Data and Code Availability

1037   Experiment code is available from https://git.mpib-berlin.mpg.de/LNDG/multi-attribute-task.
1038   Primary EEG and fMRI data (excluding structural images exempt from informed consent) will
1039   be made available following publication. Code to reproduce the analyses will be made
1040   available at https://git.mpib-berlin.mpg.de/LNDG/stateswitch.

References

Afyouni, S., & Nichols, T. E. (2018). Insight and inference for DVARS. *Neuroimage, 172,* 291-312. doi:10.1016/j.neuroimage.2017.12.098

Alitto, H., Rathbun, D. L., Vandeleest, J. J., Alexander, P. C., & Usrey, W. M. (2019). The augmentation of retinogeniculate communication during thalamic burst mode. *Journal of Neuroscience, 39*(29), 5697-5710. doi:10.1523/Jneurosci.2320-18.2019

Alnaes, D., Sneve, M. H., Espeseth, T., Endestad, T., de Pavert, S. H. P. V., & Laeng, B. (2014). Pupil size signals mental effort deployed during multiple object tracking and predicts brain activity in the dorsal attention network and the locus coeruleus. *Journal of Vision, 14*(4). doi:10.1167/14.4.1

Arcaro, M. J., Pinsk, M. A., & Kastner, S. (2015). The anatomical and functional organization of the human visual pulvinar. *Journal of Neuroscience, 35*(27), 9848-9871. doi:10.1523/Jneurosci.1575-14.2015

Aru, J., Aru, J., Priesemann, V., Wibral, M., Lana, L., Pipa, G., . . . Vicente, R. (2015). Untangling cross-frequency coupling in neuroscience. *Current Opinion in Neurobiology, 31*, 51-61. doi:10.1016/j.conb.2014.08.002

Aston-Jones, G., & Cohen, J. D. (2005). An integrative theory of locus coeruleus-norepinephrine function: Adaptive gain and optimal performance. *Annual Review of Neuroscience, 28*, 403-450. doi:10.1146/annurev.neuro.28.061604.135709

Atallah, B. V., & Scanziani, M. (2009). Instantaneous modulation of gamma oscillation frequency by balancing excitation with inhibition. *Neuron, 62*(4), 566-577. doi:10.1016/j.neuron.2009.04.027

Avants, B. B., Tustison, N. J., Song, G., Cook, P. A., Klein, A., & Gee, J. C. (2011). A reproducible evaluation of ANTs similarity metric performance in brain image registration. *Neuroimage, 54*(3), 2033-2044. doi:10.1016/j.neuroimage.2010.09.025

Bach, D. R., & Dolan, R. J. (2012). Knowing how much you don't know: A neural organization of uncertainty estimates. *Nature Reviews Neuroscience, 13*(8), 572-586. doi:10.1038/nrn3289

Bakdash, J. Z., & Marusich, L. R. (2017). Repeated measures correlation. *Frontiers in Psychology, 8*. doi:10.3389/fpsyg.2017.00456

Banca, P., Vestergaard, M. D., Rankov, V., Baek, K., Mitchell, S., Lapa, T., . . . Voon, V. (2015). Evidence accumulation in obsessive-compulsive disorder: The role of uncertainty and monetary reward on perceptual decision-making thresholds. *Neuropsychopharmacology, 40*(5), 1192-1202. doi:10.1038/npp.2014.303

Bauer, M., Kluge, C., Bach, D., Bradbury, D., Heinze, H. J., Dolan, R. J., & Driver, J. (2012). Cholinergic enhancement of visual attention and neural oscillations in the human brain. *Current Biology, 22*(5), 397-402. doi:10.1016/j.cub.2012.01.022

Beckmann, C. F., & Smith, S. A. (2004). Probabilistic independent component analysis for functional magnetic resonance imaging. *Ieee Transactions on Medical Imaging, 23*(2), 137-152. doi:10.1109/Tmi.2003.822821

Bell, A. J., & Sejnowski, T. J. (1995). An information maximization approach to blind separation and blind deconvolution. *Neural Computation, 7*(6), 1129-1159. doi:10.1162/neco.1995.7.6.1129

Berridge, C. W., & Waterhouse, B. D. (2003). The locus coeruleus-noradrenergic system: Modulation of behavioral state and state-dependent cognitive processes. *Brain Research Reviews, 42*(1), 33-84. doi:10.1016/S0165-0173(03)00143-7

Billig, A. J., Herrmann, B., Rhone, A. E., Gander, P. E., Nourski, K. V., Snoad, B. F., . . . Johnsrude, I. S. (2019). A sound-sensitive source of alpha oscillations in human non-primary auditory cortex. *Journal of Neuroscience, 39*(44), 8679-8689. doi:10.1523/Jneurosci.0696-19.2019

Birn, R. M. (2012). The role of physiological noise in resting-state functional connectivity. *Neuroimage, 62*(2), 864-870. doi:10.1016/j.neuroimage.2012.01.016

1093   Brainard, D. H. (1997). The psychophysics toolbox. *Spatial Vision, 10*(4), 433-436.
1094   doi:10.1163/156856897x00357
1095   Breton-Provencher, V., & Sur, M. (2019). Active control of arousal by a locus coeruleus
1096   GABAergic circuit. *Nature Neuroscience, 22*(2), 218-228. doi:10.1038/s41593-018-
1097   0305-z
1098   Buschman, T. J., & Kastner, S. (2015). From behavior to neural dynamics: An integrated
1099   theory of attention. *Neuron, 88*(1), 127-144. doi:10.1016/j.neuron.2015.09.017
1100   Canolty, R. T., Edwards, E., Dalal, S. S., Soltani, M., Nagarajan, S. S., Kirsch, H. E., . . .
1101   Knight, R. T. (2006). High gamma power is phase-locked to theta oscillations in
1102   human neocortex. *Science, 313*(5793), 1626-1628. doi:10.1126/science.1128115
1103   Caplan, J. B., Madsen, J. R., Raghavachari, S., & Kahana, M. J. (2001). Distinct patterns of
1104   brain oscillations underlie two basic parameters of human maze learning. *Journal of
1105   Neurophysiology, 86*(1), 368-380.
1106   Cavanagh, J. F., & Frank, M. J. (2014). Frontal theta as a mechanism for cognitive control.
1107   *Trends in Cognitive Sciences, 18*(8), 414-421. doi:10.1016/j.tics.2014.04.012
1108   Cheung, M. J., Kovacevic, N., Fatima, Z., Misic, B., & McIntosh, A. R. (2016). [MEG]PLS: A
1109   pipeline for MEG data analysis and partial least squares statistics. *Neuroimage, 124*,
1110   181-193. doi:10.1016/j.neuroimage.2015.08.045
1111   Colombo, M. A., Napolitani, M., Boly, M., Gosseries, O., Casarotto, S., Rosanova, M., . . .
1112   Sarasso, S. (2019). The spectral exponent of the resting EEG indexes the presence
1113   of consciousness during unresponsiveness induced by propofol, xenon, and
1114   ketamine. *Neuroimage, 189*, 631-644. doi:10.1016/j.neuroimage.2019.01.024
1115   Constantinople, C. M., & Bruno, R. M. (2011). Effects and mechanisms of wakefulness on
1116   local cortical networks. *Neuron, 69*(6), 1061-1068. doi:10.1016/j.neuron.2011.02.040
1117   Crick, F. (2003). Function of the thalamic reticular complex: The searchlight hypothesis.
1118   *Essential Sources in the Scientific Study of Consciousness*, 263-272.
1119   Dahl, M. J., Mather, M., Sander, M. C., & Werkle-Bergne, M. (2020). Noradrenergic
1120   responsiveness supports selective attention across the adult lifespan. *Journal of
1121   Neuroscience, 40*(22), 4372-4390. doi:10.1523/Jneurosci.0398-19.2020
1122   de Gee, J. W., Colizoli, O., Kloosterman, N. A., Knapen, T., Nieuwenhuis, S., & Donner, T. H.
1123   (2017). Dynamic modulation of decision biases by brainstem arousal systems. *Elife,
1124   6*. doi:10.7554/eLife.23232
1125   Dehghani, N., & Wimmer, R. D. (2019). A computational perspective of the role of the
1126   thalamus in cognition. *Neural Computation, 31*(7), 1380-1418.
1127   doi:10.1162/neco_a_01197
1128   Desimone, R., & Duncan, J. (1995). Neural mechanisms of selective visual-attention. *Annual
1129   Review of Neuroscience, 18*, 193-222. doi:10.1146/annurev.ne.18.030195.001205
1130   Destexhe, A., & Rudolph, M. (2004). Extracting information from the power spectrum of
1131   synaptic noise. *Journal of Computational Neuroscience, 17*(3), 327-345. doi:Doi
1132   10.1023/B:Jcns.0000044875.90630.88
1133   Destexhe, A., Rudolph, M., & Pare, D. (2003). The high-conductance state of neocortical
1134   neurons in vivo. *Nature Reviews Neuroscience, 4*(9), 739-751. doi:10.1038/nrn1198
1135   Ding, J., Sperling, G., & Srinivasan, R. (2006). Attentional modulation of SSVEP power
1136   depends on the network tagged by the flicker frequency. *Cerebral Cortex, 16*(7),
1137   1016-1029. doi:10.1093/cercor/bhj044
1138   Donner, T. H., Siegel, M., Fries, P., & Engel, A. K. (2009). Buildup of choice-predictive
1139   activity in human motor cortex during perceptual decision making. *Current Biology,
1140   19*(18), 1581-1585. doi:10.1016/j.cub.2009.07.066
1141   Dosenbach, N. U., Fair, D. A., Miezin, F. M., Cohen, A. L., Wenger, K. K., Dosenbach, R. A.,
1142   . . . Petersen, S. E. (2007). Distinct brain networks for adaptive and stable task
1143   control in humans. *Proc Natl Acad Sci U S A, 104*(26), 11073-11078.
1144   doi:10.1073/pnas.0704320104

1145 Dube, B., Emrich, S. M., & Al-Aidroos, N. (2017). More than a filter: Feature-based attention
1146   regulates the distribution of visual working memory resources. *Journal of*
1147   *Experimental Psychology-Human Perception and Performance, 43*(10), 1843-1854.
1148   doi:10.1037/xhp0000428
1149 Dugue, L., Marque, P., & VanRullen, R. (2011). The phase of ongoing oscillations mediates
1150   the causal relation between brain excitation and visual perception. *Journal of*
1151   *Neuroscience, 31*(33), 11889-11893. doi:10.1523/Jneurosci.1161-11.2011
1152 Efron, B., & Tibshirani, R. (1986). Bootstrap methods for standard errors, confidence
1153   intervals, and other measures of statistical accuracy. *Statist. Sci., 1*(1), 54-75.
1154   doi:10.1214/ss/1177013815
1155 Eickhoff, S. B., Stephan, K. E., Mohlberg, H., Grefkes, C., Fink, G. R., Amunts, K., & Zilles,
1156   K. (2005). A new SPM toolbox for combining probabilistic cytoarchitectonic maps and
1157   functional imaging data. *Neuroimage, 25*(4), 1325-1335.
1158   doi:10.1016/j.neuroimage.2004.12.034
1159 Ferguson, K. A., & Cardin, J. A. (2020). Mechanisms underlying gain modulation in the
1160   cortex. *Nature Reviews Neuroscience, 21*(2), 80-92. doi:10.1038/s41583-019-0253-y
1161 Fiebelkorn, I. C., Pinsk, M. A., & Kastner, S. (2019). The mediodorsal pulvinar coordinates
1162   the macaque fronto-parietal network during rhythmic spatial attention. *Nature*
1163   *Communications, 10.* doi:10.1038/s41467-018-08151-4
1164 Fonov, V., Evans, A. C., Botteron, K., Almli, C. R., McKinstry, R. C., Collins, D. L., & Grp, B.
1165   D. C. (2011). Unbiased average age-appropriate atlases for pediatric studies.
1166   *Neuroimage, 54*(1), 313-327. doi:10.1016/j.neuroimage.2010.07.033
1167 Forstmann, B. U., Ratcliff, R., & Wagenmakers, E. J. (2016). Sequential sampling models in
1168   cognitive neuroscience: Advantages, applications, and extensions. *Annual Review of*
1169   *Psychology, Vol 67, 67*, 641-666. doi:10.1146/annurev-psych-122414-033645
1170 Frank, M. J., Gagne, C., Nyhus, E., Masters, S., Wiecki, T. V., Cavanagh, J. F., & Badre, D.
1171   (2015). fMRI and EEG predictors of dynamic decision parameters during human
1172   reinforcement learning. *Journal of Neuroscience, 35*(2), 485-494.
1173   doi:10.1523/Jneurosci.2036-14.2015
1174 Fries, P. (2015). Rhythms for cognition: Communication through coherence. *Neuron, 88*(1),
1175   220-235. doi:10.1016/j.neuron.2015.09.034
1176 Friston, K. J., Williams, S., Howard, R., Frackowiak, R. S., & Turner, R. (1996). Movement-
1177   related effects in fMRI time-series. *Magn Reson Med, 35*(3), 346-355.
1178   doi:10.1002/mrm.1910350312
1179 Froemke, R. C. (2015). Plasticity of cortical excitatory-inhibitory balance. *Annual Review of*
1180   *Neuroscience, 38*, 195-219. doi:10.1146/annurev-neuro-071714-034002
1181 Froemke, R. C., Merzenich, M. M., & Schreiner, C. E. (2007). A synaptic memory trace for
1182   cortical receptive field plasticity. *Nature, 450*(7168), 425-429.
1183   doi:10.1038/nature06289
1184 Furey, M. L., Pietrini, P., & Haxby, J. V. (2000). Cholinergic enhancement and increased
1185   selectivity of perceptual processing during working memory. *Science, 290*(5500),
1186   2315-2319. doi:10.1126/science.290.5500.2315
1187 Gao, R., Peterson, E. J., & Voytek, B. (2017). Inferring synaptic excitation/inhibition balance
1188   from field potentials. *Neuroimage, 158*, 70-78. doi:10.1016/j.neuroimage.2017.06.078
1189 Garrett, D. D., Epp, S. M., Perry, A., & Lindenberger, U. (2018). Local temporal variability
1190   reflects functional integration in the human brain. *Neuroimage, 183*, 776-787.
1191   doi:10.1016/j.neuroimage.2018.08.019
1192 Garrett, D. D., Kovacevic, N., McIntosh, A. R., & Grady, C. L. (2010). Blood oxygen level-
1193   dependent signal variability is more than just noise. *Journal of Neuroscience, 30*(14),
1194   4914-4921. doi:10.1523/Jneurosci.5166-09.2010
1195 Garrett, D. D., McIntosh, A. R., & Grady, C. L. (2014). Brain signal variability is parametrically
1196   modifiable. *Cerebral Cortex, 24*(11), 2931-2940. doi:10.1093/cercor/bht150

1197 Garrett, D. D., Nagel, I. E., Preuschhof, C., Burzynska, A. Z., Marchner, J., Wiegert, S., . . .
1198   Lindenberger, U. (2015). Amphetamine modulates brain signal variability and working
1199   memory in younger and older adults. *Proceedings of the National Academy of*
1200   *Sciences of the United States of America, 112*(24), 7593-7598.
1201   doi:10.1073/pnas.1504090112

1202 Gold, J. I., & Shadlen, M. N. (2007). The neural basis of decision making. *Annual Review of*
1203   *Neuroscience, 30*, 535-574. doi:10.1146/annurev.neuro.29.051605.113038

1204 Grandy, T. H., Garrett, D. D., Schmiedek, F., & Werkle-Bergner, M. (2016). On the estimation
1205   of brain signal entropy from sparse neuroimaging data. *Scientific Reports, 6*.
1206   doi:10.1038/srep23073

1207 Haegens, S., Nacher, V., Luna, R., Romo, R., & Jensen, O. (2011). alpha-Oscillations in the
1208   monkey sensorimotor network influence discrimination performance by rhythmical
1209   inhibition of neuronal spiking. *Proceedings of the National Academy of Sciences of*
1210   *the United States of America, 108*(48), 19377-19382. doi:10.1073/pnas.1117190108

1211 Halassa, M. M., & Kastner, S. (2017). Thalamic functions in distributed cognitive control.
1212   *Nature Neuroscience, 20*(12), 1669-1679. doi:10.1038/s41593-017-0020-1

1213 Halassa, M. M., & Sherman, S. M. (2019). Thalamocortical circuit motifs: A general
1214   framework. *Neuron, 103*(5), 762-770. doi:10.1016/j.neuron.2019.06.005

1215 Halgren, M., Ulbert, I., Bastuji, H., Fabo, D., Eross, L., Rey, M., . . . Cash, S. S. (2019). The
1216   generation and propagation of the human alpha rhythm. *Proceedings of the National*
1217   *Academy of Sciences of the United States of America, 116*(47), 23772-23782.
1218   doi:10.1073/pnas.1913092116

1219 Hampshire, A., Chamberlain, S. R., Monti, M. M., Duncan, J., & Owen, A. M. (2010). The role
1220   of the right inferior frontal gyrus: Inhibition and attentional control. *Neuroimage, 50*(3),
1221   1313-1319. doi:10.1016/j.neuroimage.2009.12.109

1222 Hanks, T. D., & Summerfield, C. (2017). Perceptual decision making in rodents, monkeys,
1223   and humans. *Neuron, 93*(1), 15-31. doi:10.1016/j.neuron.2016.12.003

1224 Harris, K. D., & Thiele, A. (2011). Cortical state and attention. *Nature Reviews Neuroscience,*
1225   *12*(9), 509-523. doi:10.1038/nrn3084

1226 Hartings, J. A., Temereanca, S., & Simons, D. J. (2003). State-dependent processing of
1227   sensory stimuli by thalamic reticular neurons. *Journal of Neuroscience, 23*(12), 5264-
1228   5271.

1229 Hirata, A., Aguilar, J., & Castro-Alamancos, M. A. (2006). Noradrenergic activation amplifies
1230   bottom-up and top-down signal-to-noise ratios in sensory thalamus. *Journal of*
1231   *Neuroscience, 26*(16), 4426-4436. doi:10.1523/JNEUROSCI.5298-05.2006

1232 Honjoh, S., Sasai, S., Schiereck, S. S., Nagai, H., Tononi, G., & Cirelli, C. (2018). Regulation
1233   of cortical activity and arousal by the matrix cells of the ventromedial thalamic
1234   nucleus. *Nature Communications, 9*. doi:10.1038/s41467-018-04497-x

1235 Horn, A., & Blankenburg, F. (2016). Toward a standardized structural-functional group
1236   connectome in mni space. *Neuroimage, 124*, 310-322.
1237   doi:10.1016/j.neuroimage.2015.08.048

1238 Hwang, K., Bertolero, M. A., Liu, W. B., & D'Esposito, M. (2017). The human thalamus is an
1239   integrative hub for functional brain networks. *Journal of Neuroscience, 37*(23), 5594-
1240   5607. doi:10.1523/Jneurosci.0067-17.2017

1241 Iemi, L., Chaumon, M., Crouzet, S. M., & Busch, N. A. (2017). Spontaneous neural
1242   oscillations bias perception by modulating baseline excitability. *Journal of*
1243   *Neuroscience, 37*(4), 807-819. doi:10.1523/JNEUROSCI.1432-16.2016

1244 Jagtap, P., & Diwadkar, V. A. (2016). Effective connectivity of ascending and descending
1245   frontalthalamic pathways during sustained attention: Complex brain network
1246   interactions in adolescence. *Human Brain Mapping, 37*(7), 2557-2570.
1247   doi:10.1002/hbm.23196

Jaramillo, J., Mejias, J. F., & Wang, X. J. (2019). Engagement of pulvino-cortical feedforward and feedback pathways in cognitive computations. *Neuron, 101*(2), 321-336. doi:10.1016/j.neuron.2018.11.023

Jasper, H. H. (1948). Charting the sea of brain waves. *Science, 108*(2805), 343-347. doi:10.1126/science.108.2805.343

Jenkinson, M., Beckmann, C. F., Behrens, T. E., Woolrich, M. W., & Smith, S. M. (2012). Fsl. *Neuroimage, 62*(2), 782-790. doi:10.1016/j.neuroimage.2011.09.015

Jones, E. G. (2009). Synchrony in the interconnected circuitry of the thalamus and cerebral cortex. *Disorders of Consciousness, 1157*, 10-23. doi:10.1111/j.1749-6632.2009.04534.x

Joshi, S., & Gold, J. I. (2020). Pupil size as a window on neural substrates of cognition. *Trends in Cognitive Sciences, 24*(6), 466-480. doi:10.1016/j.tics.2020.03.005

Joshi, S., Li, Y., Kalwani, R. M., & Gold, J. I. (2016). Relationships between pupil diameter and neuronal activity in the locus coeruleus, colliculi, and cingulate cortex. *Neuron, 89*(1), 221-234. doi:10.1016/j.neuron.2015.11.028

Kanai, R., Komura, Y., Shipp, S., & Friston, K. (2015). Cerebral hierarchies: Predictive processing, precision and the pulvinar. *Philosophical Transactions of the Royal Society B-Biological Sciences, 370*(1668), 69-81. doi:10.1098/rstb.2014.0169

Kelly, S. P., & O'Connell, R. G. (2013). Internal and external influences on the rate of sensory evidence accumulation in the human brain. *Journal of Neuroscience, 33*(50), 19434-19441. doi:10.1523/Jneurosci.3355-13.2013

Kim, C., Cilles, S. E., Johnson, N. F., & Gold, B. T. (2012). Domain general and domain preferential brain regions associated with different types of task switching: A meta-analysis. *Human Brain Mapping, 33*(1), 130-142. doi:10.1002/hbm.21199

Kleiner, M., Brainard, D., & Pelli, D. (2007). What's new in psychtoolbox-3? *Perception, 36*, 14-14.

Klimesch, W., Sauseng, P., & Hanslmayr, S. (2007). EEG alpha oscillations: The inhibition-timing hypothesis. *Brain Res Rev, 53*(1), 63-88. doi:10.1016/j.brainresrev.2006.06.003

Kloosterman, N. A., Kosciessa, J. Q., Lindenberger, U., Fahrenfort, J. J., & Garrett, D. D. (2019). Boosting brain signal variability underlies liberal shifts in decision bias. *bioRxiv*.

Koelewijn, T., Shinn-Cunningham, B. G., Zekveld, A. A., & Kramer, S. E. (2014). The pupil response is sensitive to divided attention during speech processing. *Hearing Research, 312*, 114-120. doi:10.1016/j.heares.2014.03.010

Kosciessa, J. Q., Grandy, T. H., Garrett, D. D., & Werkle-Bergner, M. (2020). Single-trial characterization of neural rhythms: Potential and challenges. *Neuroimage, 206*, 116331. doi:10.1016/j.neuroimage.2019.116331

Kosciessa, J. Q., Kloosterman, N. A., & Garrett, D. D. (2020). Standard multiscale entropy reflects neural dynamics at mismatched temporal scales: What's signal irregularity got to do with it? *Plos Computational Biology, 16*(5), e1007885. doi:10.1371/journal.pcbi.1007885

Krishnamurthy, K., Nassar, M. R., Sarode, S., & Gold, J. I. (2017). Arousal-related adjustments of perceptual biases optimize perception in dynamic environments. *Nature Human Behaviour, 1*(6). doi:10.1038/s41562-017-0107

Krishnan, A., Williams, L. J., McIntosh, A. R., & Abdi, H. (2011). Partial least squares (PLS) methods for neuroimaging: A tutorial and review. *Neuroimage, 56*(2), 455-475. doi:10.1016/j.neuroimage.2010.07.034

Lange, J., Oostenveld, R., & Fries, P. (2013). Reduced occipital alpha power indexes enhanced excitability rather than improved visual perception. *Journal of Neuroscience, 33*(7), 3212-3220. doi:10.1523/Jneurosci.3755-12.2013

Lee, S. H., & Dan, Y. (2012). Neuromodulation of brain states. *Neuron, 76*(1), 209-222. doi:10.1016/j.neuron.2012.09.012

1301 Lendner, J. D., Helfrich, R. F., Mander, B. A., Romundstad, L., Lin, J. J., Walker, M. P., . . .
1302   Knight, R. T. (2019). An electrophysiological marker of arousal level in humans.
1303   *bioRxiv*.
1304 Lewis, L. D., Voigts, J., Flores, F. J., Schmitt, L. I., Wilson, M. A., Halassa, M. M., & Brown,
1305   E. N. (2015). Thalamic reticular nucleus induces fast and local modulation of arousal
1306   state. *Elife, 4*, e08760. doi:10.7554/eLife.08760
1307 Liu, J., Lee, H. J., Weitz, A. J., Fang, Z. N., Lin, P., Choy, M., . . . Lee, J. H. (2015).
1308   Frequency-selective control of cortical and subcortical networks by central thalamus.
1309   *Elife, 4*. doi:10.7554/eLife.09215
1310 Lopes da Silva, F. H., Vos, J. E., Mooibroek, J., & Van Rotterdam, A. (1980). Relative
1311   contributions of intracortical and thalamo-cortical processes in the generation of alpha
1312   rhythms, revealed by partial coherence analysis. *Electroencephalogr Clin*
1313   *Neurophysiol, 50*(5-6), 449-456. doi:10.1016/0013-4694(80)90011-5
1314 Lorincz, M. L., Kekesi, K. A., Juhasz, G., Crunelli, V., & Hughes, S. W. (2009). Temporal
1315   framing of thalamic relay-mode firing by phasic inhibition during the alpha rhythm.
1316   *Neuron, 63*(5), 683-696. doi:10.1016/j.neuron.2009.08.012
1317 Marguet, S. L., & Harris, K. D. (2011). State-dependent representation of amplitude-
1318   modulated noise stimuli in rat auditory cortex. *Journal of Neuroscience, 31*(17), 6414-
1319   6420. doi:10.1523/Jneurosci.5773-10.2011
1320 Maris, E., & Oostenveld, R. (2007). Nonparametric statistical testing of EEG- and MEG-data.
1321   *Journal of Neuroscience Methods, 164*(1), 177-190.
1322   doi:10.1016/j.jneumeth.2007.03.024
1323 Martins, A. R. O., & Froemke, R. C. (2015). Coordinated forms of noradrenergic plasticity in
1324   the locus coeruleus and primary auditory cortex. *Nature Neuroscience, 18*(10), 1483-
1325   1492. doi:10.1038/nn.4090
1326 Marton, T. F., Seifikar, H., Luongo, F. J., Lee, A. T., & Sohal, V. S. (2018). Roles of prefrontal
1327   cortex and mediodorsal thalamus in task engagement and behavioral flexibility.
1328   *Journal of Neuroscience, 38*(10), 2569-2578. doi:10.1523/Jneurosci.1728-17.2018
1329 Maunsell, J. H. R. (2015). Neuronal mechanisms of visual attention. *Annual Review of Vision*
1330   *Science, Vol 1, 1*, 373-391. doi:10.1146/annurev-vision-082114-035431
1331 McCormick, D. A. (1989). Cholinergic and noradrenergic modulation of thalamocortical
1332   processing. *Trends in Neurosciences, 12*(6), 215-221. doi:10.1016/0166-
1333   2236(89)90125-2
1334 McCormick, D. A., McGinley, M. J., & Salkoff, D. B. (2015). Brain state dependent activity in
1335   the cortex and thalamus. *Current Opinion in Neurobiology, 31*, 133-140.
1336   doi:10.1016/j.conb.2014.10.003
1337 McCormick, D. A., Pape, H. C., & Williamson, A. (1991). Actions of norepinephrine in the
1338   cerebral cortex and thalamus: Implications for function of the central noradrenergic
1339   system. *Prog Brain Res, 88*, 293-305. doi:10.1016/s0079-6123(08)63817-0
1340 McFadyen, J., Dolan, R. J., & Garrido, M. I. (2020). The influence of subcortical shortcuts on
1341   disordered sensory and cognitive processing. *Nature Reviews Neuroscience, 21*(5),
1342   264-276. doi:10.1038/s41583-020-0287-1
1343 McGinley, M. J., David, S. V., & McCormick, D. A. (2015). Cortical membrane potential
1344   signature of optimal states for sensory signal detection. *Neuron, 87*(1), 179-192.
1345   doi:10.1016/j.neuron.2015.05.038
1346 McGinley, M. J., Vinck, M., Reimer, J., Batista-Brito, R., Zagha, E., Cadwell, C. R., . . .
1347   McCormick, D. A. (2015). Waking state: Rapid variations modulate neural and
1348   behavioral responses. *Neuron, 87*(6), 1143-1161. doi:10.1016/j.neuron.2015.09.012
1349 McGovern, D. P., Hayes, A., Kelly, S. P., & O'Connell, R. G. (2018). Reconciling age-related
1350   changes in behavioural and neural indices of human perceptual decision-making.
1351   *Nature Human Behaviour, 2*(12), 955-966. doi:10.1038/s41562-018-0465-6

1352   McIntosh, A. R., Bookstein, F. L., Haxby, J. V., & Grady, C. L. (1996). Spatial pattern
1353   analysis of functional brain images using partial least squares. *Neuroimage, 3*(3),
1354   143-157. doi:10.1006/nimg.1996.0016
1355   McIntosh, A. R., & Lobaugh, N. J. (2004). Partial least squares analysis of neuroimaging
1356   data: Applications and advances. *Neuroimage, 23*, S250-S263.
1357   doi:10.1016/j.neuroimage.2004.07.020
1358   Minces, V., Pinto, L., Dan, Y., & Chiba, A. A. (2017). Cholinergic shaping of neural
1359   correlations. *Proceedings of the National Academy of Sciences of the United States*
1360   *of America, 114*(22), 5725-5730. doi:10.1073/pnas.1621493114
1361   Mo, C., Lu, J. S., Wu, B. C., Jia, J. R., Luo, H., & Fang, F. (2019). Competing rhythmic neural
1362   representations of orientations during concurrent attention to multiple orientation
1363   features. *Nature Communications, 10*. doi:10.1038/s41467-019-13282-3
1364   Murphy, P. R., Wilming, N., Hernandez-Bocanegra, D. C., Prat Ortega, G., & Donner, T. H.
1365   (2020). Normative circuit dynamics across human cortex during evidence
1366   accumulation in changing environments. *bioRxiv*.
1367   Nassar, M. R., Rumsey, K. M., Wilson, R. C., Parikh, K., Heasly, B., & Gold, J. I. (2012).
1368   Rational regulation of learning dynamics by pupil-linked arousal systems. *Nature*
1369   *Neuroscience, 15*(7), 1040-1046. doi:10.1038/nn.3130
1370   Nelson, S. M., Dosenbach, N. U. F., Cohen, A. L., Wheeler, M. E., Schlaggar, B. L., &
1371   Petersen, S. E. (2010). Role of the anterior insula in task-level control and focal
1372   attention. *Brain Structure & Function, 214*(5-6), 669-680. doi:10.1007/s00429-010-
1373   0260-2
1374   Ni, J. G., Wunderle, T., Lewis, C. M., Desimone, R., Diester, I., & Fries, P. (2016). Gamma-
1375   rhythmic gain modulation. *Neuron, 92*(1), 240-251. doi:10.1016/j.neuron.2016.09.003
1376   Nolan, H., Whelan, R., & Reilly, R. B. (2010). FASTER: Fully automated statistical
1377   thresholding for EEG artifact rejection. *Journal of Neuroscience Methods, 192*(1),
1378   152-162. doi:10.1016/j.jneumeth.2010.07.015
1379   O'Connell, R. G., Dockree, P. M., & Kelly, S. P. (2012). A supramodal accumulation-to-bound
1380   signal that determines perceptual decisions in humans. *Nature Neuroscience, 15*(12),
1381   1729-1735. doi:10.1038/nn.3248
1382   O'Reilly, R. C., Wyatte, D. R., & Rohrlich, J. (2017). Deep predictive learning: A
1383   comprehensive model of three visual streams. Retrieved from doi:arXiv:1709.04654
1384   Oldfield, R. C. (1971). The assessment and analysis of handedness: The edinburgh
1385   inventory. *Neuropsychologia, 9*(1), 97-113. doi:10.1016/0028-3932(71)90067-4
1386   Oostenveld, R., Fries, P., Maris, E., & Schoffelen, J. M. (2011). Fieldtrip: Open source
1387   software for advanced analysis of MEG, EEG, and invasive electrophysiological data.
1388   *Computational Intelligence and Neuroscience*. doi:10.1155/2011/156869
1389   Oostenveld, R., & Praamstra, P. (2001). The five percent electrode system for high-
1390   resolution EEG and ERP measurements. *Clinical Neurophysiology, 112*(4), 713-719.
1391   doi:10.1016/S1388-2457(00)00527-7
1392   Palva, S., & Palva, J. M. (2007). New vistas for alpha-frequency band oscillations. *Trends in*
1393   *Neurosciences, 30*(4), 150-158. doi:10.1016/j.tins.2007.02.001
1394   Parkes, L., Fulcher, B., Yucel, M., & Fornito, A. (2018). An evaluation of the efficacy,
1395   reliability, and sensitivity of motion correction strategies for resting-state functional
1396   MRI. *Neuroimage, 171*, 415-436. doi:10.1016/j.neuroimage.2017.12.073
1397   Pelli, D. G. (1997). The VideoToolbox software for visual psychophysics: Transforming
1398   numbers into movies. *Spatial Vision, 10*(4), 437-442. doi:10.1163/156856897x00366
1399   Pergola, G., Danet, L., Pitel, A. L., Carlesimo, G. A., Segobin, S., Pariente, J., . . . Barbeau,
1400   E. J. (2018). The regulatory role of the human mediodorsal thalamus. *Trends in*
1401   *Cognitive Sciences, 22*(11), 1011-1025. doi:10.1016/j.tics.2018.08.006
1402   Perrin, F., Pernier, J., Bertrand, O., & Echallier, J. F. (1989). Spherical splines for scalp
1403   potential and current-density mapping. *Electroencephalography and Clinical*
1404   *Neurophysiology, 72*(2), 184-187. doi:10.1016/0013-4694(89)90180-6

Peterson, E. J., & Voytek, B. (2017). Alpha oscillations control cortical gain by modulating excitatory-inhibitory background activity. *bioRxiv*.

Pettine, W. W., Louie, K., Murray, J. D., & Wang, X.-J. (2020). Hierarchical network model excitatory-inhibitory tone shapes alternative strategies for different degrees of uncertainty in multi-attribute decisions. *bioRxiv*.

Pfeffer, T., Avramiea, A. E., Nolte, G., Engel, A. K., Linkenkaer-Hansen, K., & Donner, T. H. (2018). Catecholamines alter the intrinsic variability of cortical population activity and perception. *Plos Biology, 16*(2), e2003453. doi:10.1371/journal.pbio.2003453

Podvalny, E., Noy, N., Harel, M., Bickel, S., Chechik, G., Schroeder, C. E., . . . Malach, R. (2015). A unifying principle underlying the extracellular field potential spectral responses in the human cortex. *Journal of Neurophysiology, 114*(1), 505-519. doi:10.1152/jn.00943.2014

Poo, C., & Isaacson, J. S. (2009). Odor representations in olfactory cortex: "Sparse" coding, global inhibition, and oscillations. *Neuron, 62*(6), 850-861. doi:10.1016/j.neuron.2009.05.022

Posner, M. I., & Rothbart, M. K. (2007). Research on attention networks as a model for the integration of psychological science. *Annual Review of Psychology, 58*, 1-23. doi:10.1146/annurev.psych.58.110405.085516

Power, J. D., Mitra, A., Laumann, T. O., Snyder, A. Z., Schlaggar, B. L., & Petersen, S. E. (2014). Methods to detect, characterize, and remove motion artifact in resting state fMRI. *Neuroimage, 84*, 320-341. doi:10.1016/j.neuroimage.2013.08.048

Rafal, R. D., & Posner, M. I. (1987). Deficits in human visual spatial attention following thalamic lesions. *Proc Natl Acad Sci U S A, 84*(20), 7349-7353. doi:10.1073/pnas.84.20.7349

Ratcliff, R. (1978). Theory of memory retrieval. *Psychological Review, 85*(2), 59-108. doi:10.1037//0033-295x.85.2.59

Ratcliff, R., & McKoon, G. (2008). The diffusion decision model: Theory and data for two-choice decision tasks. *Neural Computation, 20*(4), 873-922. doi:10.1162/neco.2008.12-06-420

Reimer, J., Froudarakis, E., Cadwell, C. R., Yatsenko, D., Denfield, G. H., & Tolias, A. S. (2014). Pupil fluctuations track fast switching of cortical states during quiet wakefulness. *Neuron, 84*(2), 355-362. doi:10.1016/j.neuron.2014.09.033

Reinagel, P., Godwin, D., Sherman, S. M., & Koch, C. (1999). Encoding of visual information by lgn bursts. *Journal of Neurophysiology, 81*(5), 2558-2569.

Richman, J. S., & Moorman, J. R. (2000). Physiological time-series analysis using approximate entropy and sample entropy. *American Journal of Physiology-Heart and Circulatory Physiology, 278*(6), H2039-H2049.

Rikhye, R. V., Gilra, A., & Halassa, M. M. (2018). Thalamic regulation of switching between cortical representations enables cognitive flexibility. *Nature Neuroscience, 21*(12), 1753-1763. doi:10.1038/s41593-018-0269-z

Rikhye, R. V., Wimmer, R. D., & Halassa, M. M. (2018). Toward an integrative theory of thalamic function. *Annual Review of Neuroscience, Vol 41, 41*, 163-183. doi:10.1146/annurev-neuro-080317-062144

Roux, F., Wibral, M., Singer, W., Aru, J., & Uhlhaas, P. J. (2013). The phase of thalamic alpha activity modulates cortical gamma-band activity: Evidence from resting-state MEG recordings. *Journal of Neuroscience, 33*(45), 17827-17835. doi:10.1523/Jneurosci.5778-12.2013

Saalmann, Y. B., & Kastner, S. (2011). Cognitive and perceptual functions of the visual thalamus. *Neuron, 71*(2), 209-223. doi:10.1016/j.neuron.2011.06.027

Saalmann, Y. B., Pinsk, M. A., Wang, L., Li, X., & Kastner, S. (2012). The pulvinar regulates information transmission between cortical areas based on attention demands. *Science, 337*(6095), 753-756. doi:10.1126/science.1223082

Sadaghiani, S., & Kleinschmidt, A. (2016). Brain networks and alpha-Oscillations: Structural and functional foundations of cognitive control. *Trends in Cognitive Sciences, 20*(11), 805-817. doi:10.1016/j.tics.2016.09.004

Schiff, N. D. (2008). Central thalamic contributions to arousal regulation and neurological disorders of consciousness. *Ann N Y Acad Sci, 1129*, 105-118. doi:10.1196/annals.1417.029

Schmitt, L. I., Wimmer, R. D., Nakajima, M., Happ, M., Mofakham, S., & Halassa, M. M. (2017). Thalamic amplification of cortical connectivity sustains attentional control. *Nature, 545*(7653), 219-223. doi:10.1038/nature22073

Sherman, S. M. (2001). Tonic and burst firing: Dual modes of thalamocortical relay. *Trends in Neurosciences, 24*(2), 122-126. doi:10.1016/S0166-2236(00)01714-8

Shine, J. M. (2019). Neuromodulatory influences on integration and segregation in the brain. *Trends in Cognitive Sciences, 23*(7), 572-583. doi:10.1016/j.tics.2019.04.002

Shine, J. M., Hearne, L. J., Breakspear, M., Hwang, K., Muller, E. J., Sporns, O., . . . Cocchi, L. (2019). The low-dimensional neural architecture of cognitive complexity is related to activity in medial thalamic nuclei. *Neuron, 104*(5), 849-855. doi:10.1016/j.neuron.2019.09.002

Siegel, M., Buschman, T. J., & Miller, E. K. (2015). Cortical information flow during flexible sensorimotor decisions. *Science, 348*(6241), 1352-1355. doi:10.1126/science.aab0551

Smith, A. M., Lewis, B. K., Ruttimann, U. E., Ye, F. Q., Sinnwell, T. M., Yang, Y. H., . . . Frank, J. A. (1999). Investigation of low frequency drift in fMRI signal. *Neuroimage, 9*(5), 526-533. doi:10.1006/nimg.1999.0435

Smith, G. D., Cox, C. L., Sherman, S. M., & Rinzel, J. (2000). Fourier analysis of sinusoidally driven thalamocortical relay neurons and a minimal integrate-and-fire-or-burst model. *Journal of Neurophysiology, 83*(1), 588-610.

Smith, S. M., Jenkinson, M., Woolrich, M. W., Beckmann, C. F., Behrens, T. E. J., Johansen-Berg, H., . . . Matthews, P. M. (2004). Advances in functional and structural MR image analysis and implementation as fsl. *Neuroimage, 23*, S208-S219. doi:10.1016/j.neuroimage.2004.07.051

Smulders, F. T. Y., ten Oever, S., Donkers, F. C. L., Quaedflieg, C. W. E. M., & van de Ven, V. (2018). Single-trial log transformation is optimal in frequency analysis of resting EEG alpha. *European Journal of Neuroscience, 48*(7), 2585-2598. doi:10.1111/ejn.13854

Song, A. H., Kucyi, A., Napadow, V., Brown, E. N., Loggia, M. L., & Akeju, O. (2017). Pharmacological modulation of noradrenergic arousal circuitry disrupts functional connectivity of the locus ceruleus in humans. *Journal of Neuroscience, 37*(29), 6938-6945. doi:10.1523/Jneurosci.0446-17.2017

Spaak, E., Bonnefond, M., Maier, A., Leopold, D. A., & Jensen, O. (2012). Layer-specific entrainment of gamma-band neural activity by the alpha rhythm in monkey visual cortex. *Current Biology, 22*(24), 2313-2318. doi:10.1016/j.cub.2012.10.020

Stitt, I., Zhou, Z. C., Radtke-Schuller, S., & Frohlich, F. (2018). Arousal dependent modulation of thalamo-cortical functional interaction. *Nature Communications, 9*(1), 2455. doi:10.1038/s41467-018-04785-6

Suffczynski, P., Kalitzin, S., Pfurtscheller, G., & da Silva, F. H. L. (2001). Computational model of thalamo-cortical networks: Dynamical control of alpha rhythms in relation to focal attention. *International Journal of Psychophysiology, 43*(1), 25-40. doi:Doi 10.1016/S0167-8760(01)00177-5

Swadlow, H. A., & Gusev, A. G. (2001). The impact of 'bursting' thalamic impulses at a neocortical synapse. *Nature Neuroscience, 4*(4), 402-408. doi:10.1038/86054

Thiele, A., & Bellgrove, M. A. (2018). Neuromodulation of attention. *Neuron, 97*(4), 769-785. doi:10.1016/j.neuron.2018.01.008

Tomasi, D., Chang, L., Caparelli, E. C., & Ernst, T. (2007). Different activation patterns for working memory load and visual attention load. *Brain Research, 1132*(1), 158-165. doi:10.1016/j.brainres.2006.11.030

Tort, A. B. L., Kramer, M. A., Thorn, C., Gibson, D. J., Kubota, Y., Graybiel, A. M., & Kopell, N. J. (2008). Dynamic cross-frequency couplings of local field potential oscillations in rat striatum and hippocampus during performance of a t-maze task. *Proceedings of the National Academy of Sciences of the United States of America, 105*(51), 20517-20522. doi:10.1073/pnas.0810524105

Twomey, D. M., Kelly, S. P., & O'Connell, R. G. (2016). Abstract and effector-selective decision signals exhibit qualitatively distinct dynamics before delayed perceptual reports. *Journal of Neuroscience, 36*(28), 7346-7352. doi:10.1523/Jneurosci.4162-15.2016

Uddin, L. Q. (2015). Salience processing and insular cortical function and dysfunction. *Nature Reviews Neuroscience, 16*(1), 55-61. doi:10.1038/nrn3857

Urai, A. E., Braun, A., & Donner, T. H. (2017). Pupil-linked arousal is driven by decision uncertainty and alters serial choice bias. *Nature Communications, 8*. doi:10.1038/ncomms14637

van Kerkoerle, T., Self, M. W., Dagnino, B., Gariel-Mathis, M. A., Poort, J., van der Togt, C., & Roelfsema, P. R. (2014). Alpha and gamma oscillations characterize feedback and feedforward processing in monkey visual cortex. *Proceedings of the National Academy of Sciences of the United States of America, 111*(40), 14332-14341. doi:10.1073/pnas.1402773111

van Vugt, M. K., Beulen, M. A., & Taatgen, N. A. (2019). Relation between centro-parietal positivity and diffusion model parameters in both perceptual and memory-based decision making. *Brain Research, 1715*, 1-12. doi:10.1016/j.brainres.2019.03.008

Vinck, M., Batista-Brito, R., Knoblich, U., & Cardin, J. A. (2015). Arousal and locomotion make distinct contributions to cortical activity patterns and visual encoding. *Neuron, 86*(3), 740-754. doi:10.1016/j.neuron.2015.03.028

Ward, L. M. (2013). The thalamus: Gateway to the mind. *Wiley Interdisciplinary Reviews-Cognitive Science, 4*(6), 609-622. doi:10.1002/wcs.1256

Waschke, L., Tune, S., & Obleser, J. (2019). Local cortical desynchronization and pupil-linked arousal differentially shape brain states for optimal sensory performance. *Elife, 8*. doi:10.7554/eLife.51501

Waterhouse, B. D., & Navarra, R. L. (2019). The locus coeruleus-norepinephrine system and sensory signal processing: A historical review and current perspectives. *Brain Res, 1709*, 1-15. doi:10.1016/j.brainres.2018.08.032

Weerda, R., Vallines, I., Thomas, J. P., Rutschmann, R. M., & Greenlee, M. W. (2006). Effects of nonspatial selective and divided visual attention on fMRI BOLD responses. *Experimental Brain Research, 173*(4), 555-563. doi:10.1007/s00221-006-0403-0

Weissman, D. H., Gopalakrishnan, A., Hazlett, C. J., & Woldorff, M. G. (2005). Dorsal anterior cingulate cortex resolves conflict from distracting stimuli by boosting attention toward relevant events. *Cerebral Cortex, 15*(2), 229-237. doi:10.1093/cercor/bhh125

Whitten, T. A., Hughes, A. M., Dickson, C. T., & Caplan, J. B. (2011). A better oscillation detection method robustly extracts EEG rhythms across brain state changes: The human alpha rhythm as a test case. *Neuroimage, 54*(2), 860-874. doi:10.1016/j.neuroimage.2010.08.064

Wiecki, T. V., Sofer, I., & Frank, M. J. (2013). HDDM: Hierarchical bayesian estimation of the drift-diffusion model in python. *Frontiers in Neuroinformatics, 7*. doi:10.3389/fninf.2013.00014

Wimmer, R. D., Schmitt, L. I., Davidson, T. J., Nakajima, M., Deisseroth, K., & Halassa, M. M. (2015). Thalamic control of sensory selection in divided attention. *Nature, 526*(7575), 705-709. doi:10.1038/nature15398

Wojciulik, E., & Kanwisher, N. (1999). The generality of parietal involvement in visual attention. *Neuron, 23*(4), 747-764. doi:10.1016/S0896-6273(01)80033-7

Wolff, M., & Vann, S. D. (2019). The cognitive thalamus as a gateway to mental representations. *Journal of Neuroscience, 39*(1), 3-14. doi:10.1523/Jneurosci.0479-18.2018

Wöstmann, M., Alavash, M., & Obleser, J. (2019). Alpha oscillations in the human brain implement distractor suppression independent of target selection. *Journal of Neuroscience, 39*(49), 9797-9805. doi:10.1523/JNEUROSCI.1954-19.2019

Wright, N. F., Vann, S. D., Aggleton, J. P., & Nelson, A. J. D. (2015). A critical role for the anterior thalamus in directing attention to task-relevant stimuli. *Journal of Neuroscience, 35*(14), 5480-5488. doi:10.1523/Jneurosci.4945-14.2015

Yang, G. J., Murray, J. D., Wang, X. J., Glahn, D. C., Pearlson, G. D., Repovs, G., . . . Anticevic, A. (2016). Functional hierarchy underlies preferential connectivity disturbances in schizophrenia. *Proceedings of the National Academy of Sciences of the United States of America, 113*(2), E219-E228. doi:10.1073/pnas.1508436113

Yizhar, O., Fenno, L. E., Prigge, M., Schneider, F., Davidson, T. J., O'Shea, D. J., . . . Deisseroth, K. (2011). Neocortical excitation/inhibition balance in information processing and social dysfunction. *Nature, 477*(7363), 171-178. doi:10.1038/nature10360

Yu, A. J., & Dayan, P. (2005). Uncertainty, neuromodulation, and attention. *Neuron, 46*(4), 681-692. doi:10.1016/j.neuron.2005.04.026

Zanto, T. P., Rubens, M. T., Thangavel, A., & Gazzaley, A. (2011). Causal role of the prefrontal cortex in top-down modulation of visual processing and working memory. *Nature Neuroscience, 14*(5), 656-U156. doi:10.1038/nn.2773

Zerbi, V., Floriou-Servou, A., Markicevic, M., Vermeiren, Y., Sturman, O., Privitera, M., . . . Bohacek, J. (2019). Rapid reconfiguration of the functional connectome after chemogenetic locus coeruleus activation. *Neuron, 103*(4), 702-718. doi:10.1016/j.neuron.2019.05.034

Supplementary Information for

Thalamocortical excitability adjustments guide human perception under uncertainty

Julian Q. Kosciessa*, Ulman Lindenberger, Douglas D. Garrett*

* Email: kosciessa@mpib-berlin.mpg.de; garrett@mpib-berlin.mpg.de

This PDF file includes:

Text S1. Parameter interrelations. To better understand individual differences in behavioral performance, we explored inter-individual associations between model parameter estimates and 'raw' median RT and mean accuracy. Linear drift rate decreases were inter-individually associated with decreases in accuracy (EEG: r = .35, p = .015, MRI: r = .46, p = .001), but not RT increases (both p > .05), whereas non-decision-time (NDT) increases tracked individual RT increases (EEG: r = .56, p = 3e-5, MRI: r = .64, p = 2e-6), but not accuracy decreases (both p > .05). For single targets, faster RTs were associated with larger drift rates (EEG: r = -.63, p = 3e-6, MRI: r = -.47, p = .002), lower non-decision times (EEG: r = .41, p = .005, MRI: r = .58, p = 3e-5), and lower boundary separation (EEG: r = .58, p = 3e-5, MRI: r = .5, p = 6e-4). More accurate performance for single targets was related to higher drift rates (EEG: r = .74, p = 3e-9; MRI: r = .79, p = 3e-10), but unrelated to boundary separation (EEG: r = .23, p = .121, MRI: r = .18, p = .244) or non-decision times (EEG: r = -.27, p = .069, MRI: r = -.38, p = .011). Amongst model parameters, we observed no parameter relations for single targets (all p > .05). However, we observed intercept-change correlations: subjects with larger drift rates for single targets exhibited strong linear drift rate reductions (EEG: r = -.93, p = 4e-22, MRI: r = -.88, p = 1e-15). Moreover, subjects with larger boundary separation showed stronger linear increases in non-decision time (r = .46, p = 9e-4, MRI: r = .59, p =2e-5). Non-decision time under selective attention, putatively dominantly reflecting visual encoding time, did not relate to changes in drift rate or NDT (both p > .05). Similarly, boundary separation did not relate to drift rate decreases (both p > .05) and drift rates under selective attention were unrelated to NDT increases (both p > .05).

Text S2. Behavioral benefits due to convergent responses. To reduce response mapping demands following probe presentation, we fixed response mapping for the two options of each feature throughout the experiment. Given that multiple attributes converge onto a similar response in a given trial, the potential to prepare motor action prior to probe presentation co-varies as a function of load. To assess the influence of this response agreement on our results, we ran an additional HDDM that simultaneously modelled both a main effect of load, as well as categorical response agreement. Notably, the obtained target load effects on drift rate and NDT were virtually identical to those observed in the selected model in both sessions (reliability of all linear effects: r >= .9 p <.001; data not shown), while linear decreases in drift and increases in NDT were also observed as a function of response divergence (i.e., lower drift and higher NDT if the probed attribute required a differential response than the other cued attributes; shown in Figure S1D for the EEG session; qualitatively similar results were obtained for MRI session; all linear effects p < .001). This suggests that response agreement systematically impacted decision processes, but cannot account for the main effects of target load. However, the large amount of added model parameters introduced partial convergence issues. We therefore chose the simpler model without response agreement for our main analyses.

Text S3. NDT increases indicate extended motor preparation demands. We observed a parametric increase in non-decision time (NDT) with target uncertainty (Figure 2B) that described shifts in RT distribution onset (Figure S3A). NDT is thought to characterize the duration of processes preceding and following evidence accumulation, i.e., probe encoding and planning/execution of the motor response. We therefore examined sensory probe- and response-related ERP components regarding their modulation by prior target uncertainty. We time-locked the CPP to the NDT group estimate for a single target – for which no button remapping was required – and (2) to the condition-wise NDT estimate. However, we observed no shift in CPP onset (Figure S3B), suggesting constant visual encoding time. To probe increases during response preparation, we assessed parametric changes in ERP amplitudes during the interval spanning the final 100 ms prior to response. This interval covered the timeframe of indicated NDT increases, after accounting for the constant probe encoding duration (Figure S3B). Notably, we observed a late frontal potential that increased in amplitude (Figure S3D) and whose onset corresponded to the temporal NDT shift (Figure S3C) after controlling for constant encoding duration (Figure S3B). This suggests that baseline NDT estimates approximate the duration of probe encoding (Nunez, Vandekerckhove, & Srinivasan, 2017), whereas NDT increases characterize increased

demands for transforming the sensory decision into a motor command (Lui et al., 2018). This further suggests that drift diffusion modelling successfully dissociated contributions from evidence integration, sensory encoding, and motor preparation. Interestingly, evidence accumulation consistently peaked at/near response execution, suggesting that additional motor demands may unravel in parallel, rather than succeed finished integration (as is often assumed in sequential sampling models).

Text S4. Behavioral PLS of spectral power during sensation. Task PLS describes the multivariate co-variation of spectral power with load. However, inter-individual behavioral differences may relate to power changes in specific bands. To probe whether inter-individual relations of power modulation to behavior would vary from the mean changes as identified via task PLS, we calculated a behavioral PLS by considering the individual linear change in spectral power with target uncertainty. This revealed a similar multivariate loading pattern as observed for the task PLS (**Figure S4B**), with high agreement between individual brainscores (r = .7, p < .001), suggesting that the identified frequency ranges jointly contributed to behavioral relations.

Text S5. Pre-stimulus alpha power increases with load, but does not relate to behavioral changes or power changes during sensation. Furthermore, decreases in pre-stimulus alpha power have been linked to increases in cortical excitability at stimulus onset (Iemi, Chaumon, Crouzet, & Busch, 2017; Lange, Oostenveld, & Fries, 2013). To probe whether expected uncertainty modulated pre-stimulus alpha power, we performed another task PLS, covering the final second of the fixation interval prior to stimulus onset. This analysis indicated that pre-stimulus alpha power increased alongside uncertainty (**Figure S4C**). Notably, in contrast to current results, elevated levels of anticipatory alpha power are often associated with decreased gamma power upon stimulus onset. Notably, linear models did not indicate associations between pre-stimulus alpha power increases across load with either drift rate decreases [r(137) = 0.02, 95%CI [-0.15, 0.18], p = 0.86], non-decision time increases [r(137) = 0.06, 95%CI [-0.1, 0.23], p = 0.45] or increases on the SPMF [r(137) = -0.13, 95%CI [-0.29, 0.04], p = 0.13]. These results are in line with increasing evidence suggesting that anticipatory alpha power modulation more closely tracks subjective confidence in upcoming decisions than sensory fidelity (Benwell et al., 2017; Limbach & Corballis, 2016).

Text S6. SSVEP magnitude is not modulated during sensation. Moreover, SSVEP magnitude has been suggested as a signature of encoded sensory information (O'Connell, Dockree, & Kelly, 2012), that is enhanced by attention (Morgan, Hansen, & Hillyard, 1996; Muller et al., 2006) and indicates fluctuations in excitability (Zhigalov, Herring, Herpers, Bergmann, & Jensen, 2019). However, despite a clear SSVEP signature, we did not observe significant effects of encoding demands on the global SSVEP magnitude (**Figure S4D**). As attentional effects on SSVEP magnitude have been shown to vary by SSVEP frequency (Ding, Sperling, & Srinivasan, 2006), the 30 Hz range may have been suboptimal here. Furthermore, the SSVEP frequency was shared across different features, thus not allowing us to assess whether uncertainty modulated the selective processing of single features. Implementing feature-specific flicker frequencies may overcome such limitations in future work, and allow to assess the changes in feature-specific processing under uncertainty.

Text S7. Rhythm-specific indices in theta and alpha band relate to multivariate spectral power modulation. Finally, as spectral power conflates rhythmic and arrhythmic signal contributions in magnitude, space and time (Kosciessa, Grandy, Garrett, & Werkle-Bergner, 2020), we performed single-trial rhythm detection, observing similar decreases in the duration and power of alpha rhythms (see **Figure S4E**) that were jointly related to stronger increases on the latent factor [duration: r(137) = -0.61, 95%CI [-0.71, -0.49], p = 1.31e-15; power: r(137) = -0.63, 95%CI [-0.72, -0.52], p = 9.66e-17]. Notably, this analysis indicated increases in theta duration, but not power, suggesting that narrowband theta power changes mainly reflected modulations in the duration of non-stationary theta rhythms, rather than changes in their strength. In line with this suggestion, increases on the spectral power factor related

to increases in theta duration [r(137) = 0.19, 95%CI [0.02, 0.35], p = 0.03], but not theta SNR [r(137) = 0.09, 95%CI [-0.08, 0.25], p = 0.31].

Text S8. A second LV may indicate decreased task engagement due to heightened difficulty at higher uncertainty levels. A 2nd significant LV (p =.012) indicated strong positive loadings in angular gyrus, middle frontal gyrus, and inferior frontal gyrus, as well as occipital cortex (see **Figure S5A**). Negative loadings were observed dominantly in medial PFC, precuneus and V5. This component increased from selective attention to target load 2, but then declined towards higher loads. Decreases in angular gyrus have been strongly to increased visual working memory load (Sheremata, Somers, & Shomstein, 2018; Todd & Marois, 2004). Increases in DMN regions, in addition to decreased prefrontal activity suggest that this component reflects relative task disengagement towards high load conditions, while increases in lateral visual cortex may reflect increased entrainment, and lack of top-down inhibition. In line with more negative loadings on this component being detrimental, we observed that inter-individually higher brainscores (i.e., positive loadings) were associated with lower non-decision times during selective attention (r = -0.46, p = .002), while stronger within-subject decreases with load were associated with larger individual NDT increases [r(122) = -0.18, 95%CI [-0.35, -0.01], p = 0.04] but not changes in drift rate [r(122) = 0.01, 95%CI [-0.17, 0.18], p = 0.95]. Larger decreases on this component were moreover related to more constrained increases in spectral modulation [r(122) = 0.39, 95%CI [0.23, 0.53], p = 6.83e-6]. Jointly, this suggests that individual drop-offs in the positive cluster of regions reflects decreased task engagement under increased difficulty, with adverse behavioral consequences.
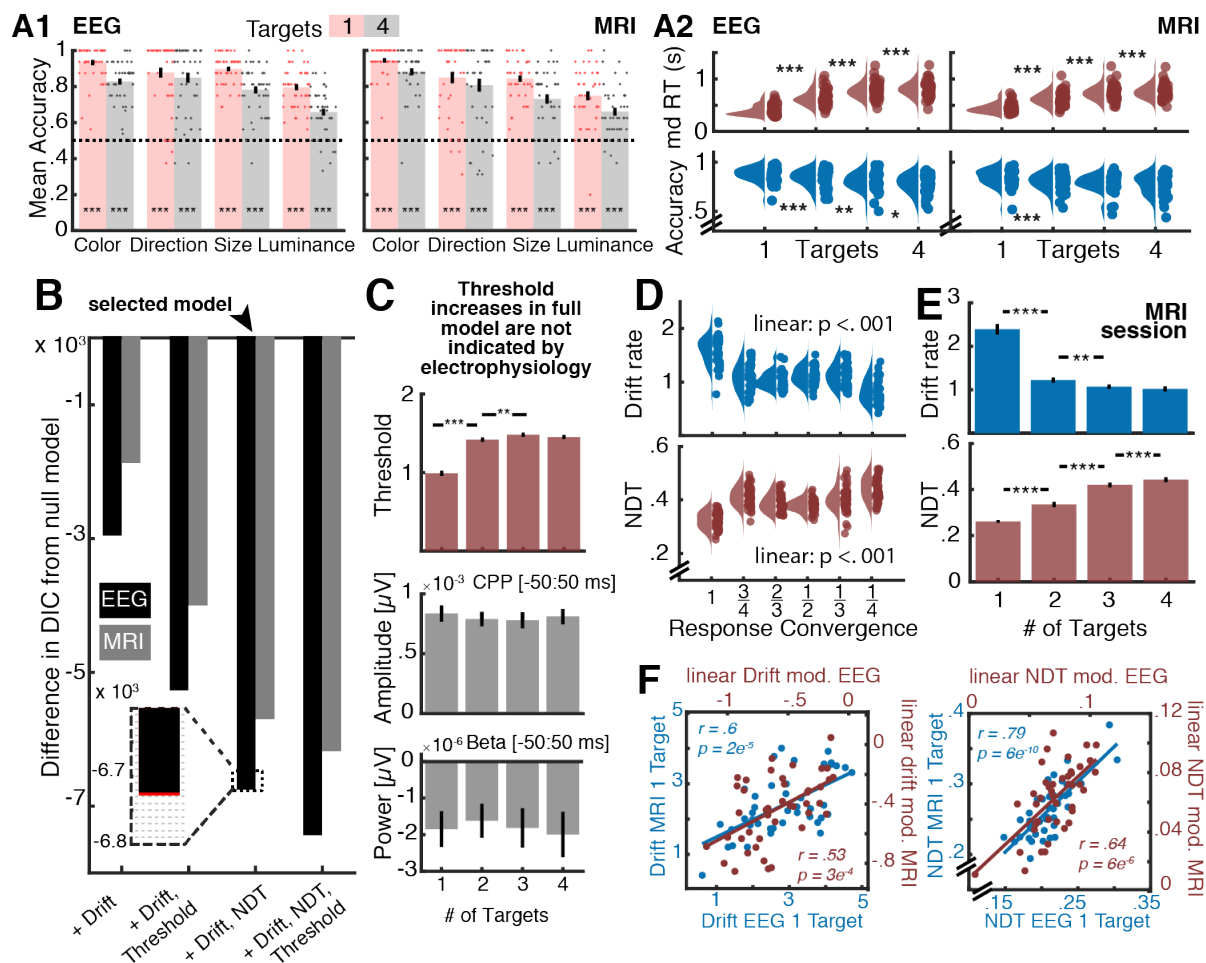
Figure S1. Additional behavioral analyses. (A1) Accuracies for single target cue and maximum target uncertainty. For all features, mean accuracy was above chance accuracy (0.5, indicated by broken lines) at the group level. Dots indicate individual accuracies. *** = p < .001 (paired t-test vs. chance accuracy). **(A2) Reaction times and accuracies by load.** All linear effects were significant (p < .001). **(B-C) HDDM model comparison. (B)** DIC-based model comparison indicates that full model, including threshold modulation, provides the best group fit to the behavioral data. However, load-related threshold increases (C) were not supported by EEG-based signatures (D). The inset shows an additional comparison of the selected model with an alternative model including starting point variation across load levels (displayed in red). Due to very constrained fit improvements, we selected the simpler model without starting point variation for further analyses. **(C) Threshold increases in full model are not indicated by electrophysiology.** The full model indicates additional threshold (also called boundary separation) increases with added target load, with qualitatively identical effects on drift rate and NDT (not shown). Boundary separation captures the conservativeness of the decision criterion and has been related to decision conflict during the choice process (e.g., Cavanagh et al., 2011). EEG-based signatures of evidence integration do not indicate threshold differences. While the full model suggested increased boundary separation, neither of the electrophysiological proxies (i.e., CPP, contralateral beta) of evidence bounds mirrors such increases. While this suggests the absence of threshold increases (McGovern, Hayes, Kelly, & O'Connell, 2018), it alternately questions the sensitivity of electrophysiological threshold estimates, which should be investigated with specific threshold modulations, such as speed-accuracy trade-off instructions, in future work. **(D) Differences in response convergence do not account for main effects of target load.** A separate model including both target load and response convergence indicated practically identical NDT and drift rate effects of target amount, while highlighting additional linear effects of response convergence. Data are individually-centered across conditions. **(E-F) Reliability of individual parameter estimates across sessions.** A separate hierarchical DDM was fit to data from each session. **(E)** Similar group-level effects were indicated for the MRI and EEG (cf. Figure 2B) session: whereas drift rate decreased with load, non-decision time increased. **(F)** Session reliability of inter-individual differences was high both for

single-target performance and for linear changes with target load. Reliability was also high for threshold estimates (r = .79, p = 6e-10). [* p <.05; ** p <.01; *** p < .001]
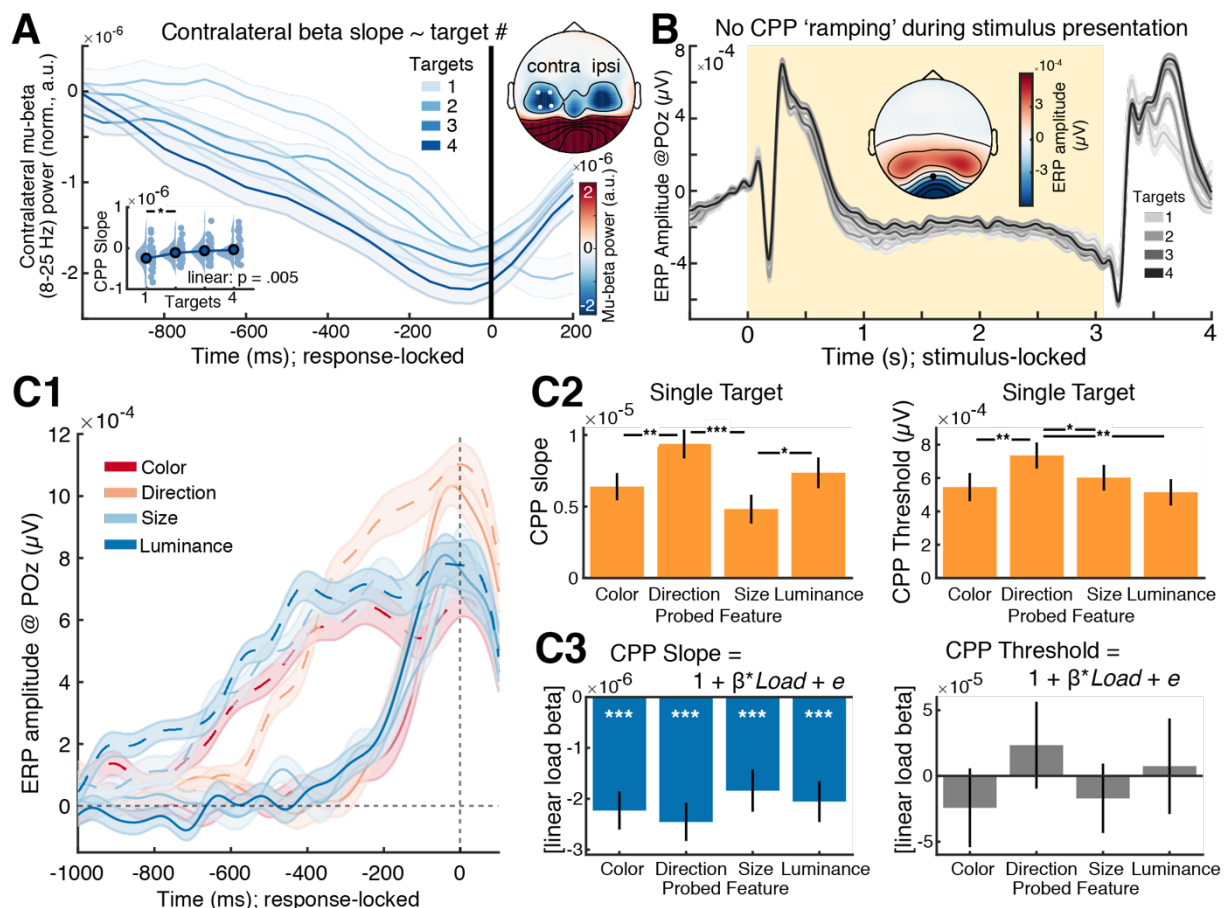
Figure S2. Additional drift rate analyses. **(A) The slope of lateralized motor preparation indicates load-related decreases in drift rate.** (A) Slopes of contralateral mu-beta power shallows with increasing attentional load levels. The inset displays linear slope estimates, estimated via linear regression from -250 ms to -50 ms, relative to response. (B) Topography of response-locked mu-beta power, averaged from -50 ms to +50 ms around response. White dots indicate the contralateral channels from which data was extracted. **(B) The centro-parietal positive potential (CPP) does not show clear ramping increases during stimulus presentation.** The yellow background indicated the stimulus presentation period. Note the modulated ramping following the probe onset at the end of stimulus presentation. The inset shows the topography of the grand average ERPs, temporally averaged during the final 2 seconds of the stimulus presentation period. The black dot indicates channel POz, at which the group-wise CPP was maximal (see Figure 2C1). **(C) Differences between probed stimulus attributes do not account for drift rate decreases under target load.** (A) Response-locked CPP as a function of probed attribute, shown for the single target (complete lines) and four target (broken lines) conditions. Data were selected by condition and probed (cf. cued), attribute, ensuring that unique trials contributed to each load condition. (B) Comparison of CPP slopes and thresholds for different probed features, when the probe target was known in advance. Slopes and thresholds were increased for direction than for other attributes, indicating relatively larger available evidence and more cautious responses (putatively 'easier' feature). (C) Load effect of CPP slopes and thresholds for different probed feature attributes. CPP slopes (i.e., evidence drift) exhibited load-related decreases for each probed attribute, whereas no threshold modulation was indicated for any of the probed attributes. [* p <.05; ** p <.01; *** p < .001]

7
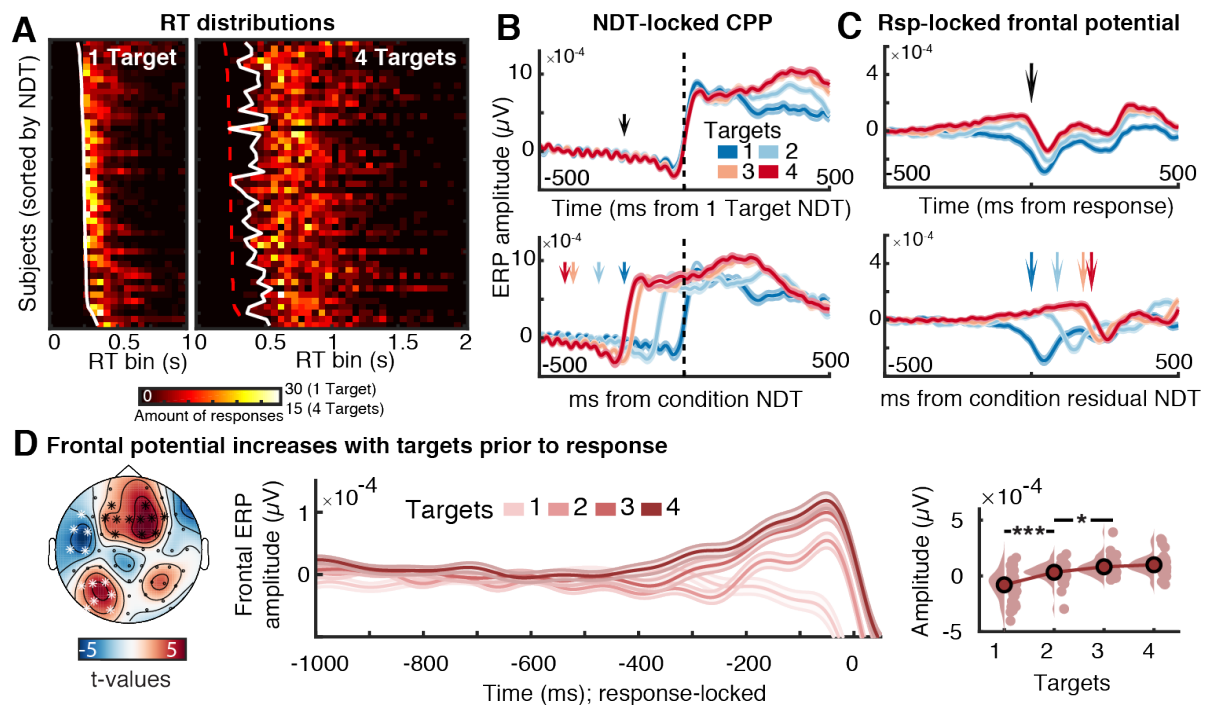
Figure S3. Non-decision time (NDT) increases putatively relate to additional motor demands, not temporal delays in CPP onset. (A) NDT estimates describe the onset of individual RT distributions (see also Lui et al., 2018). Response counts (here shown for EEG session) were sorted into 40 bins of 50 ms each. White lines indicate individual NDT estimates; the red dotted line indicates NDT estimates for the single-target condition. **(B, C) Relation of visual encoding and frontal potential to indicated NDT increases.** When response preparation can be made in advance (i.e., when only a single target is indicated) and probe onset only requires response execution, the average NDT estimate aligns with the onset of the CPP (B, top). However, load-related increases in NDT occur in the absence of temporal shifts in CPP onset (B, bottom). In C, arrows indicate the average probe onset time in each condition. In contrast, a frontal potential (see D) increases around the time of residual NDT increases (i.e., NDT estimate for each condition minus constant NDT from single-target condition; C, bottom). In D, arrows indicate the average response time in each condition. **(D) A frontal potential increase prior to response, suggesting that observed NDT increase reflect additional motor preparation demands (e.g., button remapping).** Left: Topography of test for linear ERP changes as a function of load during the final 200 ms prior to response. Clusters in white did not exhibit changes that were exclusive to the period preceding the response (data not shown). Center: Extracted traces averaged within the frontal cluster shown with black asterisks on the left. Right: Post-hoc tests on amplitudes of the frontal potential across the final 100 ms prior to response. Data are individually centered across target loads. [* p <.05; ** p <.01; *** p < .001]

8
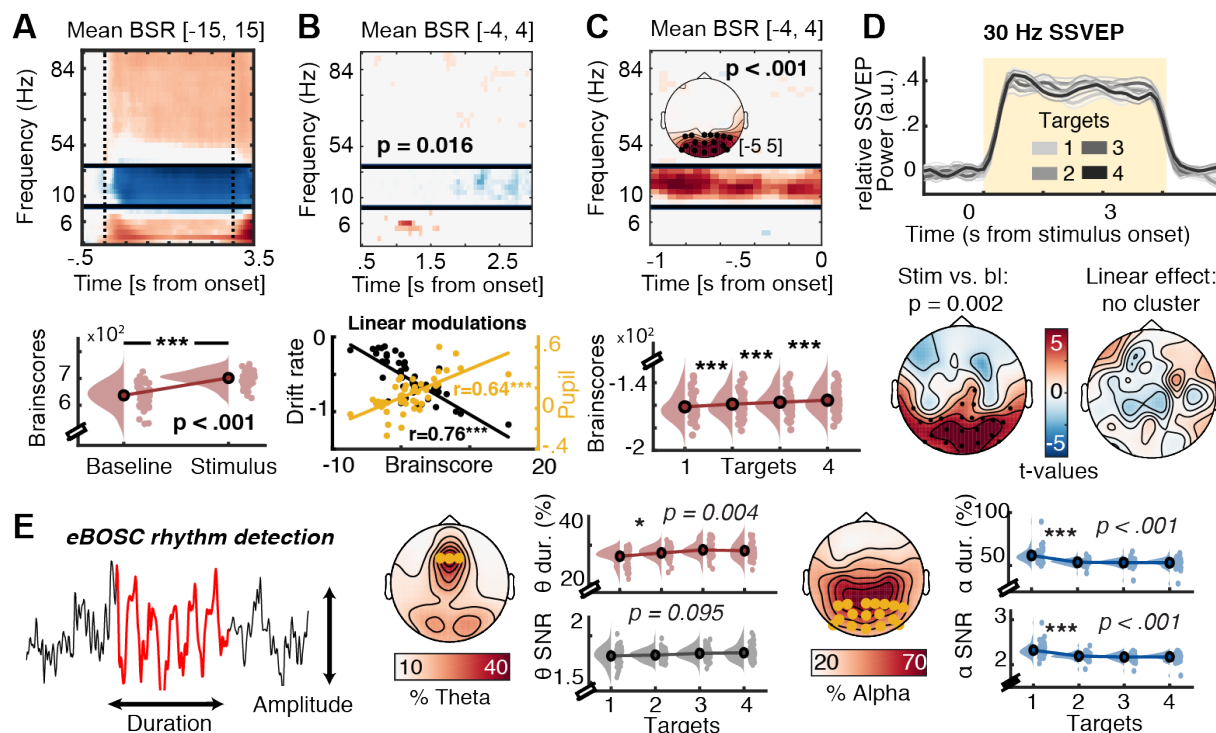
Figure S4. Additional spectral power analyses prior and during sensation. (A) Multivariate baseline changes and behavioral PLS. Note that data correspond to the different clusters indicated in Figure 3A. **(B)** Behavioral PLS, linking linear multivariate spectral power changes with target # to drift rate decreases and pupil diameter modulation. **(C) Parieto-occipital pre-stimulus alpha power increases with target load but is not related to drift changes (see Text S4). (D) SSVEP amplitude is not modulated by attentional load.** Top: Time-resolved, spectrally-normalized, SSVEP power, averaged across occipital channels (O1, Oz, O2), indicates SSVEP presence during stimulus presentation. Bottom left: Topography of stimulus-evoked SSVEP contrast minus baseline. Black dots indicate significant channels as indicated by CBPA. Bottom right: No linear load-related SSVEP modulation was indicated by CBPA. **(E) Modulation of rhythm-specific duration and power by target number.** Left: Schematic of the assessment of amplitude and duration from non-stationary rhythmic events. Right: Topographies of relative theta and alpha occurrence ('abundance'), averaged across target levels. Orange dots indicate the channels used to extract the data in E, which were the same channels also used in Figure 3AB. Target load decreased alpha duration and power and increased theta duration, but not power. Data are individually centered across target loads. [* p <.05; ** p <.01; *** p < .001]
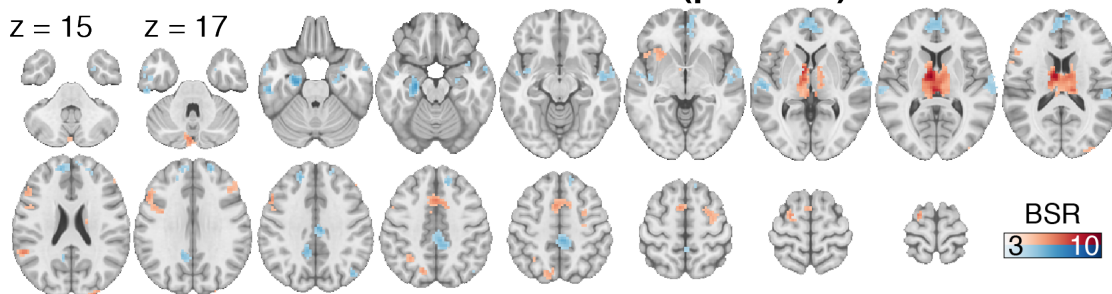
A1 Task PLS: Latent Variable 1 (p < .001)
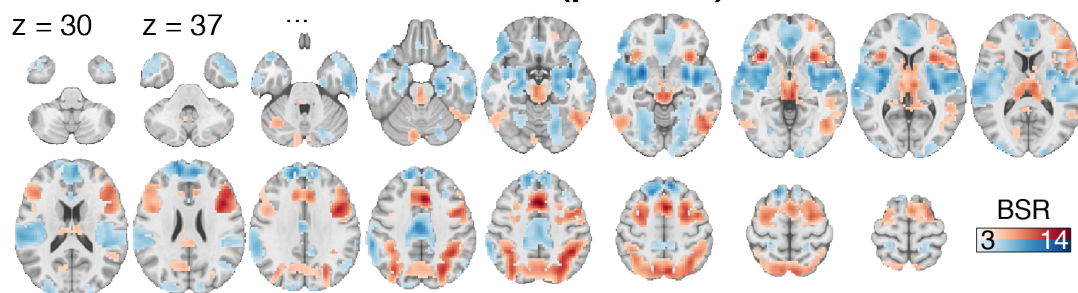
A2 Task PLS: Latent Variable 2 (p = .012)
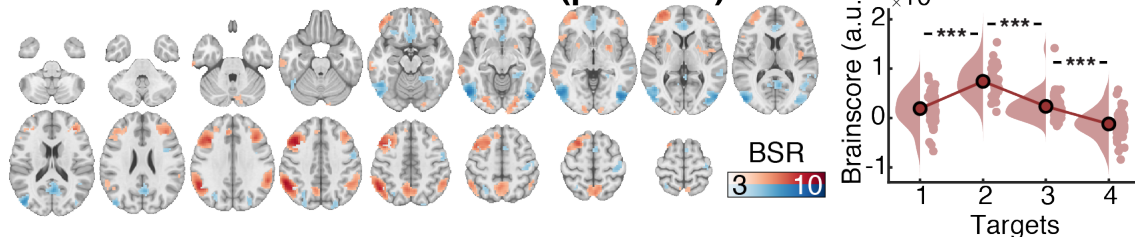
B Behavioral PLS: Latent Variable 1 (p = .001)

C Drift rate modulation: Low High
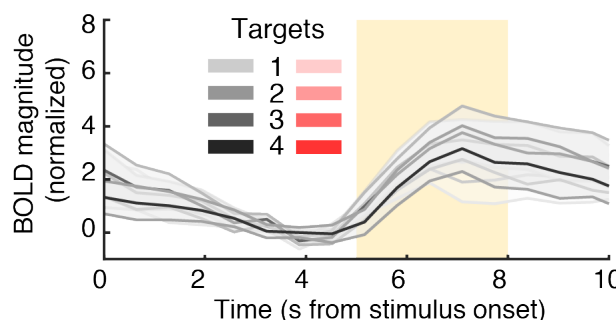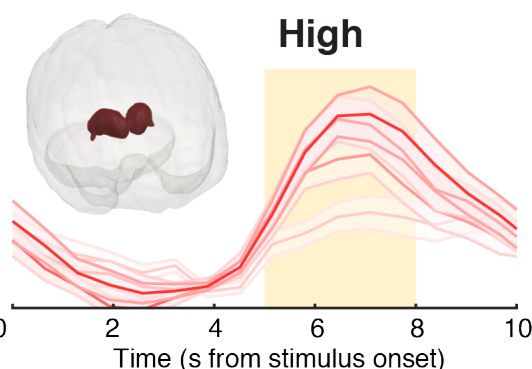
Figure S5. Additional BOLD analyses. (A, B) Full multivariate brainscore loadings for the two significant latent variables (LVs) produced by the task PLS (A) and behavioral PLS (B). (A2 left) The brainscore loadings of the second LV designate an initial increase followed by a subsequent decrease towards higher target loads. Data are individually centered across target loads. Thus, the negative components of the pattern expressed on the right become more strongly activated at low and high loads, whereas the positive components are maximally expressed when two targets are relevant. **(C) Thalamic BOLD magnitude for a median split of high- and low drift rate modulators.** The inset shows the thalamic ROI in a glass brain view. [* p <.05; ** p <.01; *** p < .001]

Table S1. PLS model peak activations, bootstrap ratios, and cluster sizes.

Model	Region	Hem	MNI Coordinates X	Y	Z	BSR	#Voxels
taskPLS LV1 BSR [-3 3]	Mid-cingulate cortex (MCC)	L	-6	15	42	13.42	2708
	Inferior Parietal Lobule (IPS)	L	-45	-45	45	11.14	2664
	Insula Lobe (anterior) [33.0 21.0 -3]	R	33	18	-3	10.86	175
	Inferior Occipital Gyrus [-54 -69 -12]	L	-57	-69	-12	10.1	702
	Thalamus [-8 -27 -2]	L	-6	-30	-3	9.93	1121
	Superior Frontal Gyrus	R	27	-3	54	9.47	880
	Inferior Temporal Gyrus	R	51	-60	-12	6.72	265
	Superior Orbital Gyrus	L	-27	54	-3	6.2	232
	Cerebellum (Crus 1)	R	6	-81	-24	6.12	109
	PCC [-6.0 -35.0 28.0]	L	-9	-33	27	5.72	62
	Cerebellum (VI)	R	30	-63	-30	5.64	59
	Cerebellar Vermis (9)		0	-57	-36	4.32	32
	Cerebellum (Crus 2)	L	-6	-84	-33	3.82	26
	Pallidum [24.0 3.0 -6.0]; bilateral	R	24	0	-9	-11.74	3882
	Insula Lobe	L	-33	-18	6	-11.05	3776
	Superior Frontal Gyrus	L	-12	36	54	-10.6	2096
	MCC	L	0	-15	36	-9.72	706
	Lingual Gyrus	R	21	-84	-6	-7.43	440
	Superior Occipital Gyrus	R	27	-96	15	-5.54	318
	Middle Frontal Gyrus	L	-33	24	39	-5.48	44
	Angular Gyrus	L	-48	-63	27	-5.31	106
	Superior Parietal Lobule	L	-21	-45	63	-5.12	94
	Postcentral Gyrus	R	21	-39	63	-4.98	89
BSR [-6 6] (additional clusters that were merged in +/- 3 threshold)	IFG	L	-45	9	30	12.576	790
	Insula Lobe	L	-33	18	-3	10	93
	IFG	R	42	27	18	7	32
	IFG	R	51	33	-9	-8.69	125
	SMG	R	57	-39	39	-7.80	56
	Inferior Temporal Gyrus	L	-57	-6	-33	-7.57	96
taskPLS LV2	Angular Gyrus	R	54	-51	36	8.69	638
	Middle Frontal Gyrus	R	39	18	39	8.24	1238
	IFG (p. Orbitalis)	R	42	45	-12	6.37	141
	SupraMarginal Gyrus	L	-60	-45	33	6.36	317
	Middle Frontal Gyrus	L	-42	24	33	6.21	477
	Inferior Occipital Gyrus	L	-27	-90	-12	5.66	110
	Precuneus	R	3	-60	45	5.54	383
	Middle Temporal Gyrus	R	60	-33	-12	5.26	154
	IFG (p. Triangularis)	R	48	18	3	5.07	115
	Lingual Gyrus	R	21	-84	-6	4.99	77
	Putamen	L	-30	3	-3	4.62	115
	Cerebelum (Crus 2)	L	-9	-81	-27	4.22	34
	Putamen	R	24	0	6	3.93	30
	Inferior Occipital Gyrus	L	-48	-75	-6	-7.92	378
	Inferior Occipital Gyrus	R	51	-72	-15	-7.61	706
	Olfactory cortex	L	-3	18	-12	-5.63	502
	Precuneus	L	-6	-63	21	-5.56	220
	Superior Parietal Lobule	R	27	-54	63	-4.46	39
	Fusiform Gyrus	L	-24	-45	-15	-4.43	83
	Postcentral Gyrus	L	-57	-3	42	-4.38	58
	Postcentral Gyrus	L	-45	-27	57	-4.36	85
	Superior Orbital Gyrus	R	21	27	-15	-4.32	25
	Superior Occipital Gyrus	R	27	-69	36	-4.29	58
	Precentral Gyrus	L	-42	0	30	-4.23	28
	Middle Temporal Gyrus	L	-54	-57	12	-4.18	38
			-69	-42	9	-4.13	51
	Middle Occipital Gyrus	L	-30	-81	36	-4.1	60
	Posterior-Medial Frontal	L	-6	6	60	-3.95	33
	Hippocampus	L	-27	-18	-21	7.04	111

behavioral PLS: LV1	Inferior Temporal Gyrus [-56 -24 -30]	L	-57	-24	-30	5.5	40
	Superior Medial Gyrus	R	3	63	15	5.43	345
	ParaHippocampal Gyrus	R	21	-12	-24	5.35	35
	MCC	R	3	-33	48	5.3	174
	Middle Temporal Gyrus	L	-60	0	-30	4.77	27
	MCC	L	-12	-45	36	4.72	64
	Superior Frontal Gyrus	R	18	51	30	4.68	33
	Fusiform Gyrus	R	24	12	-45	4.67	30
	Middle Temporal Gyrus	R	57	-3	-15	4.64	239
	Superior Frontal Gyrus	L	-21	42	36	4.61	26
	Superior Temporal Gyrus	L	-57	-21	3	4.6	61
	Angular Gyrus	R	39	-72	39	4.59	36
	Middle Temporal Gyrus	L	-51	-3	-21	4.52	72
	Temporal Pole	R	36	6	-21	4.42	25
	Superior Medial Gyrus	L	9	36	45	4.25	29
	Thalamus	L	-9	-9	12	-9.73	591
	Superior Frontal Gyrus	L	-24	-3	69	-5.59	38
	Posterior-Medial Frontal	L	-3	15	45	-5.22	154
	Superior Occipital Gyrus	R	27	-96	21	-5.15	39
	SupraMarginal Gyrus	L	-60	-48	24	-5.13	28
	Cerebelum (Crus 2)	L	-6	-84	-33	-5.09	35
	Superior Parietal Lobule	L	-18	-69	48	-5.07	36
	IFG (p. Opercularis)	L	-57	15	33	-4.87	173
	Insula Lobe	L	-30	21	-3	-4.37	44
	Inferior Parietal Lobule	L	-33	-54	45	-4.03	30
	Superior Frontal Gyrus	R	24	0	54	-3.9	51
	Middle Frontal Gyrus	R	45	36	33	-3.78	35

Note: Locations where peaks had to be shifted for a label are indicated with coordinates in the label.

Supplementary References

Benwell, C. S. Y., Tagliabue, C. F., Veniero, D., Cecere, R., Savazzi, S., & Thut, G. (2017). Prestimulus EEG power predicts conscious awareness but not objective visual performance. *Eneuro, 4*(6). doi:10.1523/ENEURO.0182-17.2017

Cavanagh, J. F., Wiecki, T. V., Cohen, M. X., Figueroa, C. M., Samanta, J., Sherman, S. J., & Frank, M. J. (2011). Subthalamic nucleus stimulation reverses mediofrontal influence over decision threshold. *Nature Neuroscience, 14*(11), 1462-1467. doi:10.1038/nn.2925

Ding, J., Sperling, G., & Srinivasan, R. (2006). Attentional modulation of SSVEP power depends on the network tagged by the flicker frequency. *Cerebral Cortex, 16*(7), 1016-1029. doi:10.1093/cercor/bhj044

Iemi, L., Chaumon, M., Crouzet, S. M., & Busch, N. A. (2017). Spontaneous neural oscillations bias perception by modulating baseline excitability. *Journal of Neuroscience, 37*(4), 807-819. doi:10.1523/JNEUROSCI.1432-16.2016

Kosciessa, J. Q., Grandy, T. H., Garrett, D. D., & Werkle-Bergner, M. (2020). Single-trial characterization of neural rhythms: Potential and challenges. *Neuroimage, 206*, 116331. doi:10.1016/j.neuroimage.2019.116331

Lange, J., Oostenveld, R., & Fries, P. (2013). Reduced occipital alpha power indexes enhanced excitability rather than improved visual perception. *Journal of Neuroscience, 33*(7), 3212-3220. doi:10.1523/Jneurosci.3755-12.2013

Limbach, K., & Corballis, P. M. (2016). Prestimulus alpha power influences response criterion in a detection task. *Psychophysiology, 53*(8), 1154-1164. doi:10.1111/psyp.12666

Lui, K. K., Nunez, M. D., Cassidy, J. M., Vandekerckhove, J., Cramer, S. C., & Srinivasan, R. (2018). Timing of readiness potentials reflect a decision-making process in the human brain. *bioRxiv*.

McGovern, D. P., Hayes, A., Kelly, S. P., & O'Connell, R. G. (2018). Reconciling age-related changes in behavioural and neural indices of human perceptual decision-making. *Nature Human Behaviour, 2*(12), 955-966. doi:10.1038/s41562-018-0465-6

Morgan, S. T., Hansen, J. C., & Hillyard, S. A. (1996). Selective attention to stimulus location modulates the steady-state visual evoked potential. *Proceedings of the National Academy of Sciences of the United States of America, 93*(10), 4770-4774. doi:10.1073/pnas.93.10.4770

Muller, M. M., Andersen, S., Trujillo, N. J., Valdes-Sosa, P., Malinowski, P., & Hillyard, S. A. (2006). Feature-selective attention enhances color signals in early visual areas of the human brain. *Proceedings of the National Academy of Sciences of the United States of America, 103*(38), 14250-14254. doi:10.1073/pnas.0606668103

Nunez, M. D., Vandekerckhove, J., & Srinivasan, R. (2017). How attention influences perceptual decision making: Single-trial EEG correlates of drift-diffusion model parameters. *Journal of Mathematical Psychology, 76*, 117-130. doi:10.1016/j.jmp.2016.03.003

O'Connell, R. G., Dockree, P. M., & Kelly, S. P. (2012). A supramodal accumulation-to-bound signal that determines perceptual decisions in humans. *Nature Neuroscience, 15*(12), 1729-+. doi:10.1038/nn.3248

Sheremata, S. L., Somers, D. C., & Shomstein, S. (2018). Visual short-term memory activity in parietal lobe reflects cognitive processes beyond attentional selection. *Journal of Neuroscience, 38*(6), 1511-1519. doi:10.1523/Jneurosci.1716-17.2017

Todd, J. J., & Marois, R. (2004). Capacity limit of visual short-term memory in human posterior parietal cortex. *Nature, 428*(6984), 751-754. doi:10.1038/nature02466

Zhigalov, A., Herring, J. D., Herpers, J., Bergmann, T. O., & Jensen, O. (2019). Probing cortical excitability using rapid frequency tagging. *Neuroimage, 195*, 59-66. doi:10.1016/j.neuroimage.2019.03.056